

<https://doi.org/10.1038/s41545-024-00393-8>

# Synergistic mechanisms of novel Z-Scheme N,S co-doped biochar-based $\text{Ag}_3\text{PO}_4$ composites for efficient removal of norfloxacin

Check for updates

Tongtong Wang<sup>1,2</sup>✉, Amit Kumar<sup>3</sup>, Gaurav Sharma<sup>3</sup>, Sen Wang<sup>4</sup>, Junchao Jia<sup>5</sup>, Jiyong Zheng<sup>2</sup> & Hui Shi<sup>1,6</sup>✉

In this study, a novel N, S-co-doped carbon-based  $\text{Ag}_3\text{PO}_4$  composite photocatalyst (N,S- $\text{Ag}_3\text{PO}_4@\text{ACB}$ ) was synthesized using activated biochar (ACB) as a carrier and used for the efficient removal of norfloxacin (NOR), a typical bio-refractory antibiotic. We systematically investigated the degradation effects, actual wastewater treatment, the impacts of environmental factors, and the degradation pathways. The results show that N,S- $\text{Ag}_3\text{PO}_4@\text{ACB}$  is essentially a p-n heterojunction with Z-scheme of  $\text{Ag}_2\text{S}/\text{Ag}_3\text{PO}_4/\text{ACB}$  composite containing Ag nanoparticles. After 120 min of irradiation, N,S- $\text{Ag}_3\text{PO}_4@\text{ACB}$  removed 90.42% of an initial NOR concentration of  $50 \text{ mg L}^{-1}$ . The activation of graphitic N and the lone electron pairs of N and S, promoted rapid photogenerated charge transfer. Furthermore, the surface properties of ACB promoted free radicals generation, and the surface plasmon resonance effect of the Ag nanoparticles synergistically enhanced the photocatalytic activity. A new degradation intermediate of NOR was identified, and the degradation dynamics were elucidated with three main pathways.

The excessive use and unchecked disposal of antibiotics can cause water and environmental pollution, which can hinder social and economic development<sup>1</sup>. Norfloxacin (NOR), a third-generation quinolone antibiotic, is widely used in the medical, aquatic, and animal husbandry industries because of its good pharmacokinetic properties, low cost, excellent antimicrobial properties, and ability to be used in conjunction with other antibiotics without cross-infection<sup>2,3</sup>. However, NOR cannot be fully metabolized in living organisms and has a long half-life in the environment, resulting in easy accumulation especially in surface water, groundwater, and even drinking water<sup>4</sup>, which has been detected in many countries around the world<sup>3</sup>. Residual NOR is highly toxic; for example, it induces heart disease, stroke, and other diseases, causing resistance genes and bacterial genotoxicity<sup>5</sup>. Thus, methods for removing NOR from aqueous environments must be urgently developed<sup>6</sup>. Photocatalysis is one of the most effective and promising technologies for the degradation of antibiotics<sup>4</sup>. Extensive research showed that the development of semiconductors and

composite materials with a visible-light response is essential for real applications<sup>7</sup>. Silver phosphate ( $\text{Ag}_3\text{PO}_4$ ) is an important silver N-type semiconductor with strong photo-oxidation properties and a high quantum yield under visible light irradiation and has attracted significant attention<sup>8</sup>.  $\text{Ag}_3\text{PO}_4$ , from the cubic crystal system, absorbs  $<530 \text{ nm}$  visible light with a suitable band gap (2.36–2.43 eV) and a deep valence band (approximately +2.90 eV) relative to the normal hydrogen electrode (NHE,  $\text{pH}=0$ ), making it suitable for oxidation reactions<sup>8,9</sup>. This is attributed to the introduction of p-region Group VA non-metallic P elements into  $\text{Ag}_2\text{O}$ , forming stable  $\text{PO}_4$  tetrahedra in  $\text{Ag}_3\text{PO}_4$  and modifying the energy band edge<sup>10</sup>. However, the micro solubility of  $\text{Ag}_3\text{PO}_4$  in water and the photocorrosion phenomenon caused the loss of photocatalysts, which affected the activity and stability of photocatalysis, thus limiting its large-scale application<sup>11</sup>.

Researchers have developed cost-effective methods to improve the visible-light photocatalytic performance of  $\text{Ag}_3\text{PO}_4$ , including construction of heterojunctions via composites with carbon materials<sup>9</sup>, elemental

<sup>1</sup>Institute for Interdisciplinary and Innovate Research, Xi'an University of Architecture and Technology, Xi'an, PR China. <sup>2</sup>State Key Laboratory of Soil Erosion and Dryland Farming on the Loess Plateau, Northwest A & F University, Yangling, PR China. <sup>3</sup>International Research Centre of Nanotechnology for Himalayan Sustainability (IRCNHS), Shoolini University, Solan, India. <sup>4</sup>School of Resources Engineering, Xi'an University of Architecture and Technology, Xi'an, PR China. <sup>5</sup>Bio-Agriculture Institute of Shaanxi, Shaanxi Province Academy of Sciences, Xi'an, PR China. <sup>6</sup>School of Environmental and Municipal Engineering, Xi'an University of Architecture and Technology, Xi'an, PR China. ✉e-mail: [tongtwang@163.com](mailto:tongtwang@163.com); [wangtongtong@xauat.edu.cn](mailto:wangtongtong@xauat.edu.cn); [shihui@xauat.edu.cn](mailto:shihui@xauat.edu.cn)

doping<sup>10</sup>, and structural modulation<sup>12</sup>. Biochar is a low-cost, green mesoporous carbon material with abundant environmentally persistent free radicals (EPFRs), surface oxygen-containing functional groups (OFGs), and unique defects<sup>13</sup>; thus, it is used as a carrier or co-catalyst for mediating a variety of catalytic reactions<sup>14</sup>. Wei et al.<sup>15</sup> synthesized biochar-based  $\text{Ag}_3\text{PO}_4$  photocatalysts via the ball milling-pyrolysis-precipitation method and explored the effects and mechanisms of synergistic adsorption-photocatalytic removal of methylene blue. Nevertheless, this preparation method is cumbersome and this cationic dye is highly photosensitive, and the initial concentration selected is low, resulting in significant removal. Wang et al.<sup>9</sup> further found that biochar-based  $\text{Ag}_3\text{PO}_4$  composites were easily prepared using a co-precipitation method and that the porous structure and surface properties of the carriers (biochar) contributed to the enhancement of pollutant adsorption, hence the excellent removal of cationic dyes at high concentrations. However, the previous research suffers from too long degradation time for antibiotics. To further enhance the photocatalytic activity of biochar-based  $\text{Ag}_3\text{PO}_4$  composites, numerous studies have focused on the design strategies of metal-ion doping<sup>16</sup>, polymer composites<sup>17</sup>, or composites with metal-type semiconductors to construct heterojunctions<sup>18,19</sup>. Qian et al.<sup>20</sup> used hydrothermal impregnation to incorporate biochar into  $\text{Ag}_3\text{PO}_4/\alpha\text{-Fe}_2\text{O}_3$  heterojunctions to enhance the generation of reactive oxygen species (ROS) and application in the degradation of low concentrations of tetracycline and ciprofloxacin ( $20 \text{ mg L}^{-1}$ ). Unfortunately, these reports still lack a systematic elaboration of the mechanisms of enhanced photocatalytic roles and probing evidence of the synergistic effects of dopant ions<sup>21</sup>. Furthermore, these methods mainly targeted non-antibiotic organic pollutants. Additionally, when investigating the degradation of antibiotics, the environmental impact was not comprehensively evaluated, limiting the removal of antibiotics at high initial concentrations, thus limiting their industrial applications<sup>9</sup>.

Another important design strategy involves activating Ag-based composite photocatalysts using non-metal ion doping<sup>22</sup>. However, the studies are not comprehensive<sup>11,21</sup>; therefore, the design of composite photocatalysts based on this strategy should be further investigated to improve the efficiency of environmental applications and promote green development. Common non-metallic doping includes C, N, S, B, and other heteroatoms; these dopants may modulate the interaction forces between the material skeleton and the molecules<sup>22</sup>. Additionally, co-doping of two heteroatoms may further modulate the chemical composition and porous structure of materials<sup>23</sup>. Currently, the most remarkable applications are N and S co-doped carbon materials, which are attributed to the synergistic effects between N and S<sup>24</sup>. Mao et al.<sup>25</sup> prepared an N and S co-doped biochar-based  $\text{Bi}_2\text{WO}_6$  composite that exhibited excellent performance in reducing the band gap energy and promoting photogenerated carrier separation. Shabir et al.<sup>26</sup> suggested that co-doping effectively lowers the bandgap of  $\text{TiO}_2$  and reduces the recombination rate between photo-generated electrons and holes, while the doped material serves as an active site for adsorbing pollutants for photodegradation<sup>23</sup>. Moreover, owing to the synergistic effect of numerous ions in co-doping, the light absorption range increases, thus enhancing photocatalysis. However, the synergistic mechanism and influencing process need to be discussed in detail<sup>27</sup>. Thus far, few studies have been conducted on N and S co-doped biochar-based  $\text{Ag}_3\text{PO}_4$  composite photocatalysts. Additionally, there are few studies on the photocatalytic removal of NOR at high concentrations and the synergistic mechanisms of N and S co-doping. Therefore, in this study, a novel N, S co-doped biochar-based  $\text{Ag}_3\text{PO}_4$  composite photocatalyst (N,S- $\text{Ag}_3\text{PO}_4$ @ACB) was prepared via hydrothermal synthesis and chemical co-precipitation method using thiourea as the precursor. First, several advanced methods were used to characterize the physicochemical and optical properties of N,S- $\text{Ag}_3\text{PO}_4$ @ACB. Thereafter, the application of N,S- $\text{Ag}_3\text{PO}_4$ @ACB for NOR degradation and wastewater treatment was investigated, along with its recyclability and photostability. Subsequently, the photogenerated carrier behavior of N,S- $\text{Ag}_3\text{PO}_4$ @ACB was analyzed using electrochemistry; the main active species were identified via capture experiments. The mechanisms through which N, S co-doping

synergistically enhanced photocatalysis were elucidated. Finally, the dynamic degradation transformation of NOR by N,S- $\text{Ag}_3\text{PO}_4$ @ACB was explored using three-dimensional excitation-emission matrix fluorescence spectra (3D EEMs), and the possible degradation pathways of NOR were elucidated employing high performance liquid chromatography-mass spectrometry (HPLC-MS). This paper is expected to introduce new perspectives on the photocatalytic mechanisms of N, S co-doping and biochar synergistic enhancement of Ag-system semiconductors, as well as provide key research ideas for the degradation process of NOR and newly identified degradation intermediates.

## Methods

### Chemical reagents

Silver nitrate ( $\text{AgNO}_3$ ), sodium phosphate dibasic ( $\text{Na}_2\text{HPO}_4$ ), thiourea ( $\text{CH}_4\text{N}_2\text{S}$ ), NOR ( $\text{C}_{16}\text{H}_{18}\text{FN}_3\text{O}_3$ ), potassium hydroxide (KOH), sodium hydroxide (NaOH), hydrochloric acid (HCl), p-benzoquinone (BQ), *tert*-butyl alcohol (TBA), ammonium oxalate (AO), manganese acetate (MA), and common solvents were used in this study and were ordered from Sinopharm Chemical Reagent Co., Ltd (Shanghai, China). Ultrapure water was employed throughout the experiments. All chemicals and solvents were of analytical grade and did not require further purification.

### Preparation of N,S- $\text{Ag}_3\text{PO}_4$ @ACB

To obtain biochar, *Caragana korshinskii* biomass (collected from Guyuan City, Ningxia Autonomous Region, China) was sheared and pyrolyzed at  $650^\circ\text{C}$  for 3 h in an argon atmosphere. Subsequently, the activated *Caragana korshinskii* biochar (ACB) was obtained via ultrasonic activation combined with KOH pore-making treatment at  $700^\circ\text{C}$  for 1 h to remove impurities. All temperatures were increased at  $5^\circ\text{C min}^{-1}$  in an argon atmosphere.

$\text{AgNO}_3$  ( $25 \text{ mL}$ ,  $0.2 \text{ mol L}^{-1}$ ) was added to ACB ( $1.00 \text{ g}$ ) and the mixture was ultrasonicated for 1 h, and was further stirred for 1 h. Thiourea ( $0.60 \text{ g}$ ) and  $100 \text{ mL}$  of ultrapure water were added and ultrasonicated for 30 min. Following this, the mixture was transferred to a Teflon<sup>™</sup>-equipped autoclave (SLM 250, Beijing Sen Long Reactor Co., Ltd, China) with a controlled fill ratio of  $\sim 60\%$  and hydrothermally reacted at  $105^\circ\text{C}$  for 3 h (with stirring). After cooling, the mixture was removed from the autoclave, and  $25 \text{ mL}$  of  $\text{AgNO}_3$  was added; the mixture was ultrasonicated for 1 h and further stirred for 1 h. In an environment protected from light,  $9 \text{ mL}$  of  $\text{Na}_2\text{HPO}_4$  ( $0.2 \text{ mol L}^{-1}$ ) was added dropwise to the abovementioned mixture with constant stirring, followed by ultrasonication at  $50^\circ\text{C}$  for 2 h and stirring for 2 h. Finally, the mixture was suction-filtered and activated in an oven at  $80^\circ\text{C}$  to obtain the solid N,S- $\text{Ag}_3\text{PO}_4$ @ACB, which was ground and passed through a  $0.15 \text{ mm}$  mesh sieve. The control materials  $\text{Ag}_3\text{PO}_4$  and  $\text{Ag}_3\text{PO}_4$ @ACB were prepared similarly. The simple N,S- $\text{Ag}_3\text{PO}_4$ @ACB preparation procedure is illustrated in Fig. 1.

### Experiments and characterization

The removal effects of N,S- $\text{Ag}_3\text{PO}_4$ @ACB on NOR in an aqueous solution and actual wastewater were investigated via typical adsorption-degradation experiments. Three parallel and control tests were set up for all experiments. Important experimental parameters are labeled in the figure of the result analysis. X-ray diffraction (XRD), Scanning electron microscopy (SEM), transmission electron microscopy (TEM), high-resolution TEM (HRTEM), Fourier-transform infrared (FTIR), Raman spectroscopy, ultraviolet-visible/diffuse reflectance spectroscopy (UV-vis/DRS), X-ray photoelectron spectroscopy (XPS), the Brunauer-Emmett-Teller (BET) specific surface area ( $S_{\text{BET}}$ ) and pore size analysis, three-dimensional excitation-emission matrix fluorescence spectra (3D EEMs), inductively coupled plasma mass spectrometry (ICP-MS), steady-state photoluminescence (PL) spectroscopy, photoelectrochemical properties including transient photocurrent response (PC) and electrochemical impedance spectroscopy (EIS), and electron spin resonance (ESR) were performed in this work. The detailed experimental procedures, material characterizations (to investigate the basic physico-chemical properties, structure, morphology, surface characteristics,

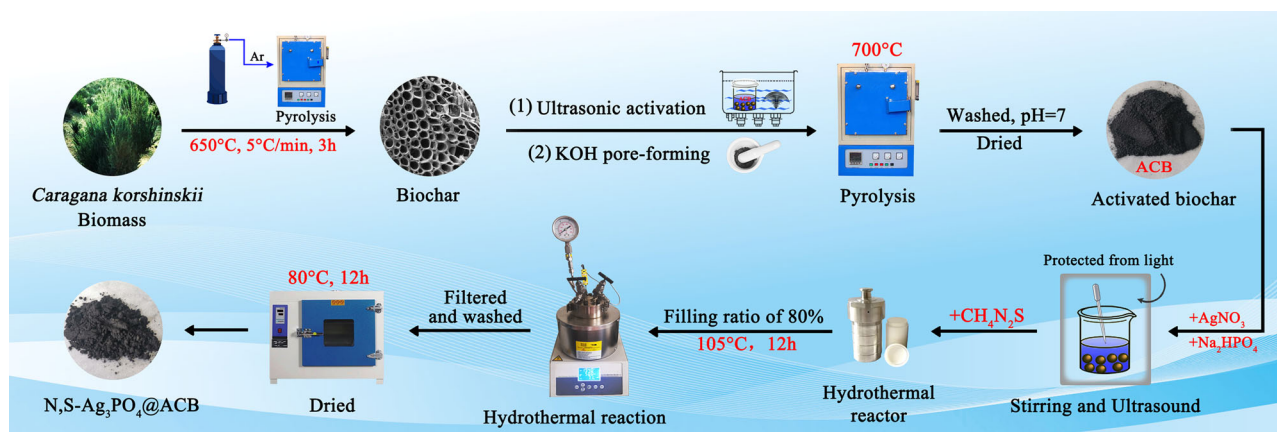


Fig. 1 | Schematic illustration of the synthesis of N,S-Ag<sub>3</sub>PO<sub>4</sub>@ACB in this study.

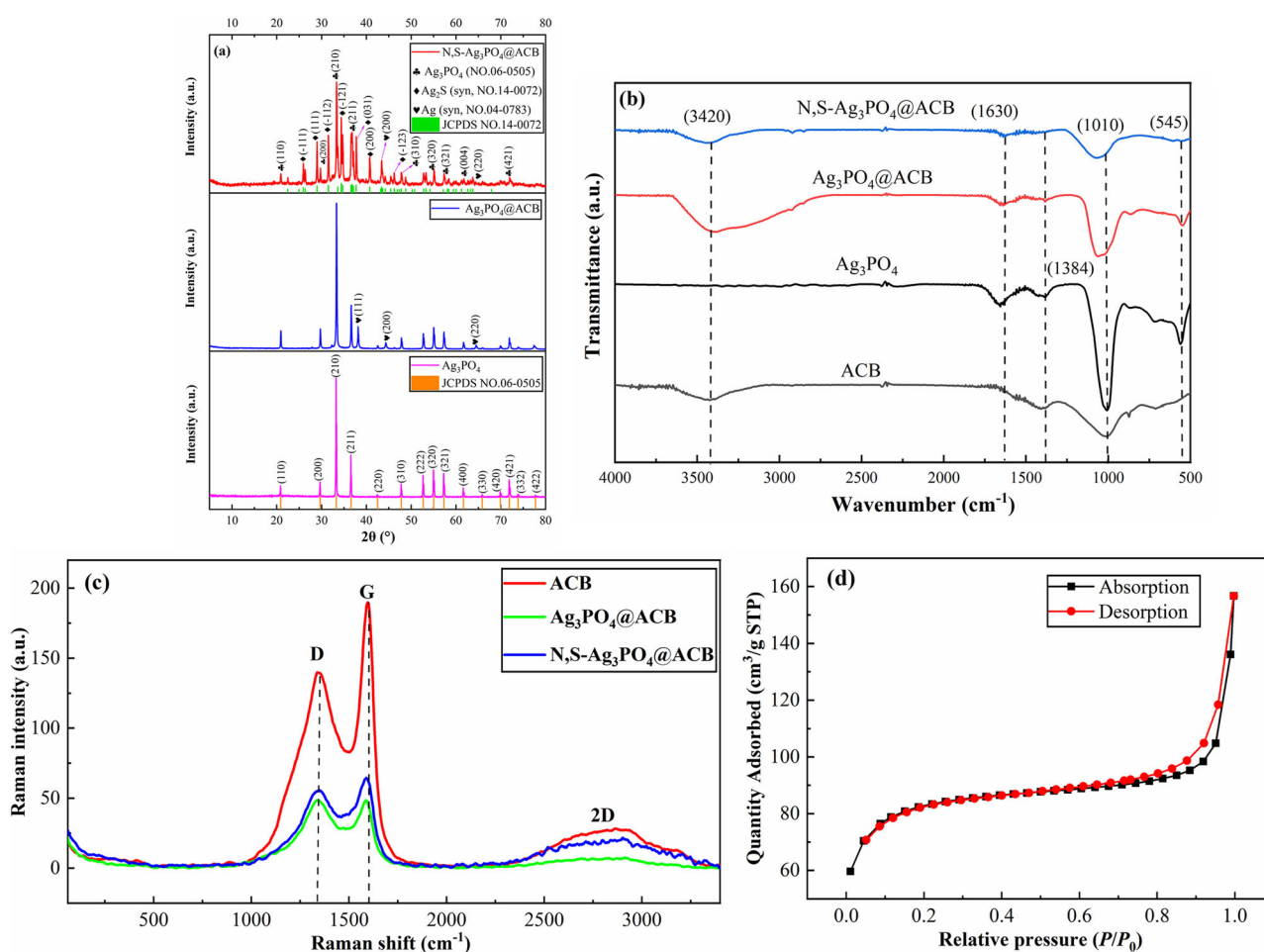


Fig. 2 | XRD patterns, FTIR, Raman spectroscopy, and adsorption-desorption isotherm of the prepared photocatalysts. **a** XRD patterns, **b** FTIR spectra, **c** Raman spectra, and **d** adsorption-desorption isotherm of N,S-Ag<sub>3</sub>PO<sub>4</sub>@ACB.

and optical behavior of the prepared materials, etc.), and analysis methods can be found in a previously published paper<sup>29</sup>.

## Results and discussions

### Characterization

The XRD patterns of both Ag<sub>3</sub>PO<sub>4</sub>@ACB and N,S-Ag<sub>3</sub>PO<sub>4</sub>@ACB were indexed to the cubic phase crystal Ag<sub>3</sub>PO<sub>4</sub> (JCPDS No. 06-0505), and the corresponding crystal faces were labeled (Fig. 2a). Additionally,  $2\theta = 25.9^\circ$ ,

$28.9^\circ$ ,  $31.5^\circ$ ,  $34.4^\circ$ ,  $40.7^\circ$ ,  $43.4^\circ$ , and  $46.2^\circ$  were matched to the monoclinic phase crystal Ag<sub>2</sub>S, which corresponded to the crystal planes (-111), (111), (-112), (-121), (-121), (031), (200), and (-123), respectively. The diffraction peak of Ag<sub>2</sub>S was relatively weak compared to that of Ag<sub>3</sub>PO<sub>4</sub>, matching the standard structure of JCPDS No. 14-0072<sup>28</sup>. Moreover, the peaks of  $2\theta$  at  $40.3^\circ$  and  $64.4^\circ$  were fitted to the (200) and (220) planes of the cubic phase crystal Ag nanoparticles (JCPDS No. 04-0783) with a space group of Fm-3m(225). This may imply that some of the Ag<sup>+</sup> was reduced to Ag

**Table 1 | Basic physico-chemical properties of the prepared materials**

Photocatalysts	C (%) <sup>a</sup>	Ag (%)	O (%)	P (%)	N (%)	S (%)	S <sub>BET</sub> (m <sup>2</sup> ·g <sup>-1</sup> )	Pore volume <sup>c</sup> (cm <sup>3</sup> ·g <sup>-1</sup> )	Pore size <sup>d</sup> (nm)
ACB	85.42	– <sup>b</sup>	11.52	–	0.76	–	995.70	0.463	1.86
Ag <sub>3</sub> PO <sub>4</sub>	–	77.31	15.29	7.40	–	–	21.73	0.001	11.90
Ag <sub>3</sub> PO <sub>4</sub> @ACB	72.87	12.49	12.86	1.11	0.67	–	148.19	0.092	2.49
N,S-Ag <sub>3</sub> PO <sub>4</sub> @ACB	64.37	12.41	13.86	1.79	2.03	5.54	304.00	0.162	2.13

<sup>a</sup>These data are from EDS energy spectra.

<sup>b</sup>“–” means have not been detected or not determined.

<sup>c</sup>Single point adsorption total pore volume.

<sup>d</sup>Adsorption average pore diameter (4V/S<sub>BET</sub>).

monomers during ternary complexation<sup>29</sup>. Diffraction peaks of ACB were not detected because of the Ag<sub>2</sub>S/Ag<sub>3</sub>PO<sub>4</sub> coverage, and the ACB exhibited an amorphous state. Therefore, N,S-Ag<sub>3</sub>PO<sub>4</sub>@ACB is a Ag<sub>2</sub>S/Ag<sub>3</sub>PO<sub>4</sub>/ACB heterogeneous photocatalyst that contains a few reduced Ag nanoparticles. Notably, S in thiourea chemically reacts with Ag via a hydrothermal reaction to produce Ag<sub>2</sub>S crystals.

FTIR (Fig. 2b) and Raman (Fig. 2c) spectra were employed to analyze the surface functional group and defect structure of the materials. The FTIR spectra of Ag<sub>3</sub>PO<sub>4</sub>@ACB and N,S-Ag<sub>3</sub>PO<sub>4</sub>@ACB were similar (Fig. 2b), and the typical infrared features of both ACB and Ag<sub>3</sub>PO<sub>4</sub> were detected. Specifically, the broad –OH stretching vibrational peak near 3420 cm<sup>-1</sup> is attributed to ACB, and the strong vibrational peaks near 1010 and 545 cm<sup>-1</sup> are attributed to the P–O stretching vibration of PO<sub>4</sub><sup>3-</sup> from Ag<sub>3</sub>PO<sub>4</sub>. Moreover, ACB exhibits C–O stretching vibration at 1010 cm<sup>-1</sup>, but when ACB is complexed with Ag<sub>3</sub>PO<sub>4</sub>, this characteristic peak redshifts slightly to 1070 cm<sup>-1</sup> owing to superposition. Additionally, the characteristic peak at 1630 cm<sup>-1</sup> may be an O–H bending vibrational peak from the adsorbed water of Ag<sub>3</sub>PO<sub>4</sub>, and the characteristic peak at 1384 cm<sup>-1</sup> may correspond to a C=O bond from ACB<sup>19</sup>. However, all these characteristic peaks of N,S-Ag<sub>3</sub>PO<sub>4</sub>@ACB were slightly weakened by N and S co-doping.

There was no marked difference in the positions of the D and 2D bands of Ag<sub>3</sub>PO<sub>4</sub>@ACB compared with those of the characteristic peaks of ACB (Fig. 2c). The G band, which represents graphitic carbon, was slightly blue-shifted, probably owing to the interaction of Ag<sub>3</sub>PO<sub>4</sub> with the graphitized structure of ACB. The intensities of these peaks were significantly weakened, indicating the combination of Ag<sub>3</sub>PO<sub>4</sub> with the multilayer graphitized structure of ACB. With N and S co-doping, the D and G bands of N,S-Ag<sub>3</sub>PO<sub>4</sub>@ACB were strengthened considerably, and the ratio of the D peak intensity to the G peak intensity was slightly higher than that of Ag<sub>3</sub>PO<sub>4</sub>@ACB. This observation indicates a higher degree of defects and disorder in the carbon crystals of N,S-Ag<sub>3</sub>PO<sub>4</sub>@ACB, which may have facilitated the separation of photogenerated carriers therein. Mao et al.<sup>25</sup> also suggested that co-doping with N and S affects the degree of defects in biochar; S may facilitate efficient chemical reactivity, whereas N may directly interact with carbon atoms to alter electrical conductivity.

The specific surface areas, pore volumes, and pore sizes are listed in Table 1 and Supplementary Table 1. Figure 2d shows the adsorption-desorption isotherm, demonstrating that N,S-Ag<sub>3</sub>PO<sub>4</sub>@ACB exits a hysteresis loop at relative pressures of 0.60 to 0.95, which is a typical feature of mesoporous structures. The BET-specific surface area (S<sub>BET</sub>) of Ag<sub>3</sub>PO<sub>4</sub>@ACB was 148.19 m<sup>2</sup> g<sup>-1</sup>, which is much less than that of ACB. When N and S were co-doped, the S<sub>BET</sub> of N,S-Ag<sub>3</sub>PO<sub>4</sub>@ACB instead increased to 304.00 m<sup>2</sup> g<sup>-1</sup>, which also increased the pore volume to 0.162 cm<sup>3</sup> g<sup>-1</sup> and decreased the average pore diameter to 2.13 nm. This suggests that the co-doping of N and S activated the pore structure of Ag<sub>3</sub>PO<sub>4</sub>@ACB, leading to redistribution of the Ag<sub>3</sub>PO<sub>4</sub> crystals on the surface of ACB, and improved the active sites of N,S-Ag<sub>3</sub>PO<sub>4</sub>@ACB<sup>30</sup>.

Field Emission Scanning Electron Microscopy (FESEM, Fig. 3) and Transmission Electron Microscopy (TEM, Fig. 4) with an energy-dispersive spectrometer (EDS, Table 1) enable the visualization of the microscopic morphology of the materials. The ACB had a porous honeycomb structure with a smooth surface and many exposed pore channels (Fig. 3a). Ag<sub>3</sub>PO<sub>4</sub>

displayed irregular particles and was densely embedded in the porous structure of the ACB. The growth of cubic crystals on the inner wall of the ACB may be attributed to electrostatically driven self-assembly between Ag<sup>+</sup> and the negatively charged ACB on the surface<sup>9</sup>. Additional FESEM images are provided in Supplementary Fig. 1. Figure 3b indicates a similar morphology, with many crystal particles deposited inside the ACB pores. Figure 3c shows finer Ag<sub>2</sub>S microspheres stacked on Ag<sub>3</sub>PO<sub>4</sub> particles to form a similar core-shell structure<sup>26</sup>, which implies that the Ag<sub>2</sub>S/Ag<sub>3</sub>PO<sub>4</sub> combination was loaded together into the porous structure of the ACB. It is also possible that Ag<sub>2</sub>S/Ag<sub>3</sub>PO<sub>4</sub> was most probably deposited separately on the surface of the thin layer of ACB (Fig. 3d). This is different from the Ag<sub>3</sub>PO<sub>4</sub>@ACB morphology (Fig. 3a), implying that the co-doping of N and S led to the formation of Ag<sub>2</sub>S/Ag<sub>3</sub>PO<sub>4</sub> heterojunctions. To further verify the distribution of Ag<sub>2</sub>S/Ag<sub>3</sub>PO<sub>4</sub> in this composite, elemental mapping was performed, as shown in Fig. 3e. It clearly shows that C, Ag, O, P, and S were uniformly distributed in N,S-Ag<sub>3</sub>PO<sub>4</sub>@ACB, confirming the formation of a heterojunction. Moreover, the relatively high level of S, whose distribution was similar to that of Ag, confirmed the production of Ag<sub>2</sub>S in the hydrothermal reaction.

ACB existed in the form of folded sheets, and Ag<sub>3</sub>PO<sub>4</sub> and Ag<sub>2</sub>S were anchored on top of these folded sheets to aggregate and form deep black lattice spots (Fig. 4a). The lattice spacings of 0.2689 and 0.2454 nm in Fig. 4b may be assigned to the (210) and (211) planes of Ag<sub>3</sub>PO<sub>4</sub>, respectively, and the lattice spacing of 0.2836 nm matches the (–112) plane of Ag<sub>2</sub>S. The Ag<sub>2</sub>S/Ag<sub>3</sub>PO<sub>4</sub> crystals were closely surrounded by the ACB interface, which indicates that the Ag<sub>2</sub>S and Ag<sub>3</sub>PO<sub>4</sub> crystals are very close to each other and that the ternary heterojunction of Ag<sub>2</sub>S/Ag<sub>3</sub>PO<sub>4</sub>/ACB was successfully constructed. This was confirmed by the HRTEM images of the other investigated regions (Fig. 4c), where the (210) plane of Ag<sub>3</sub>PO<sub>4</sub> and the (–112) plane of Ag<sub>2</sub>S were observed. Figure 4d displays a selected area electron diffraction (SAED) image of N,S-Ag<sub>3</sub>PO<sub>4</sub>@ACB, which shows that the composite photocatalyst was polycrystalline<sup>31</sup>. The (–112) and (040) planes of Ag<sub>2</sub>S and (110), (210), and (220) planes of Ag<sub>3</sub>PO<sub>4</sub> were identified. Thus, these micromorphological characterizations further confirm that N,S-Ag<sub>3</sub>PO<sub>4</sub>@ACB is essentially a composite Ag<sub>2</sub>S/Ag<sub>3</sub>PO<sub>4</sub>/ACB heterojunction.

Figure 5 shows the XPS spectra to characterize the bonded valence structure of N,S-Ag<sub>3</sub>PO<sub>4</sub>@ACB. The survey spectra of this composite detected P 2p, S 2p, C 1s, Ag 3d, N 1s, O 1s, and followed by typical Ag 3p double peaks<sup>32</sup>, which further validated the co-doping of N, S into Ag<sub>3</sub>PO<sub>4</sub>@ACB. The binding energies corresponding to the valence states of these elements are labeled in Fig. 5a with atomic percentages matching the EDS results (Table 1). The high-resolution spectra of C 1s (Fig. 5b) could be deconvoluted to three peaks at 284.8, 286.4, and 288.9 eV, corresponding to the carbon material backbones C–C, C–O/C–N, and O–C=O bonds, respectively, derived from ACB<sup>18</sup>. The O 1s high-resolution spectra (Fig. 5c) show two fitted peaks at 530.5 and 532.1 eV, which are attributed to lattice oxygen and adsorbed oxygen (–OH), respectively. In Fig. 5d, Ag 3d may be deconvoluted into four fitted peaks, with two strong characteristic peaks near 368.1 and 374.1 eV corresponding with Ag 3d<sub>5/2</sub> and Ag 3d<sub>3/2</sub> in Ag<sub>3</sub>PO<sub>4</sub> (or Ag<sub>2</sub>S), respectively, indicating the presence of Ag<sup>+</sup> in the composite<sup>28</sup>. Additionally, two weak peaks near 369.4 and 372.9 eV were

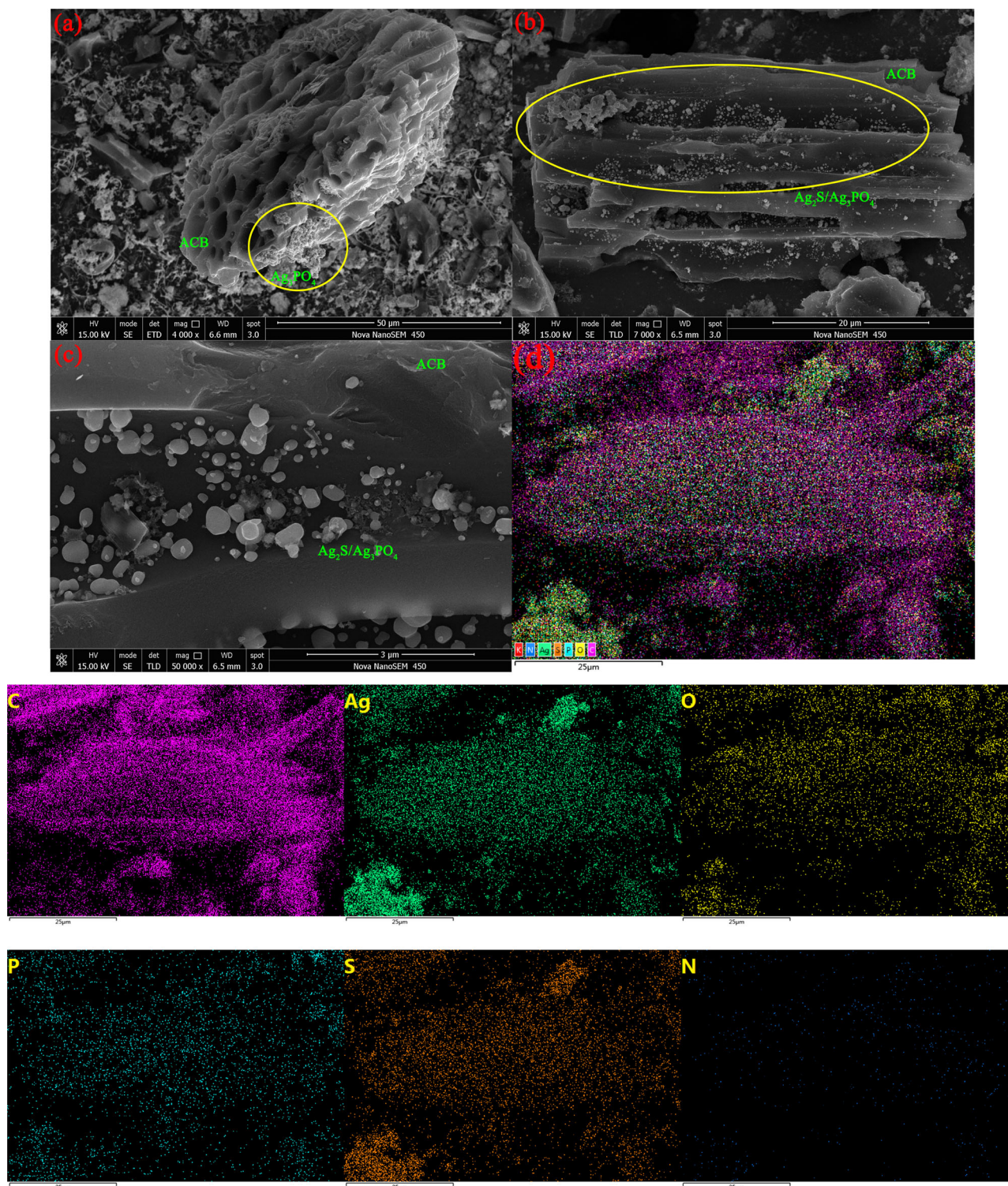
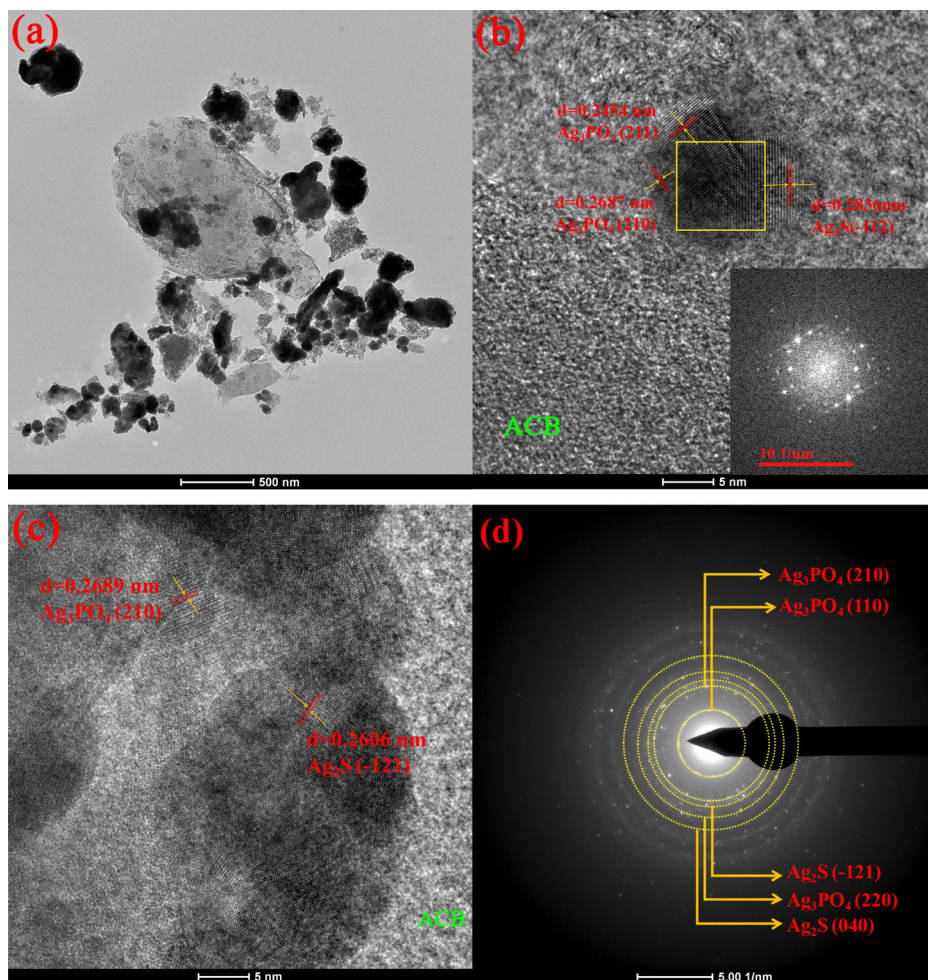


**Fig. 3 | FESEM and mapping images of the prepared photocatalysts. a** FESEM image of  $\text{Ag}_3\text{PO}_4@\text{ACB}$ , **b, c** FESEM images of  $\text{N,S-Ag}_3\text{PO}_4@\text{ACB}$ , and **d** FESEM-mapping mixed total image of  $\text{N,S-Ag}_3\text{PO}_4@\text{ACB}$ , followed by the distribution maps of each element as C, Ag, O, P, S, and N, respectively.

attributed to nano  $\text{Ag}^0$  monomers, which is consistent with the XRD analysis of  $\text{Ag}/\text{Ag}_2\text{S}/\text{Ag}_3\text{PO}_4$  that is complexed to the ACB surface. In the S 2p spectra (Fig. 5e), the  $\text{S}2p_{3/2}$  and  $\text{S}2p_{1/2}$  peaks at  $\sim 161.2$  and  $162.4$  eV support the valence state of  $\text{S}^{2-}$ , and the doublet separation energy of  $1.2$  eV is consistent with the valence characterization of the metal sulfides attributed to  $\text{Ag}_2\text{S}$ <sup>33</sup>. The P 2p peak at  $132.5$  eV (Fig. 5f) indicates that P had a +5 valence state, which was attributed to the valence state of  $\text{P}^{5+}$  in  $\text{Ag}_3\text{PO}_4$ <sup>32</sup>. As

shown in Fig. 5g, the N 1s separable peaks were fitted to two peaks at  $398.2$  and  $400.8$  eV, corresponding to C–N bonds and graphitized N, respectively. This implies that N doping mainly activates the biochar and affects the C atoms, all of which contribute to the defect structure of the ACB. Moreover, graphitized N facilitates the supply of active sites to enhance photoelectron migration in photocatalysis<sup>25</sup>. The XPS results further confirm that the N,S co-doped  $\text{Ag}_3\text{PO}_4@\text{ACB}$  is a heterostructure of  $\text{Ag}/\text{Ag}_2\text{S}/\text{Ag}_3\text{PO}_4/\text{ACB}$ .

**Fig. 4 | TEM and HRTEM images of N,S-Ag<sub>3</sub>PO<sub>4</sub>@ACB. a** TEM image of N,S-Ag<sub>3</sub>PO<sub>4</sub>@ACB, **b, c** HRTEM images of N,S-Ag<sub>3</sub>PO<sub>4</sub>@ACB, and **d** SAED of N,S-Ag<sub>3</sub>PO<sub>4</sub>@ACB.



### Optical properties

As illustrated in Fig. 6a, the maximum absorbance edge of Ag<sub>3</sub>PO<sub>4</sub> was ~534 nm, and both Ag<sub>3</sub>PO<sub>4</sub>@ACB and N,S-Ag<sub>3</sub>PO<sub>4</sub>@ACB exhibited excellent absorption in the range of 200–800 nm. Moreover, with N and S co-doping, the average absorbance of N,S-Ag<sub>3</sub>PO<sub>4</sub>@ACB (curve above) was substantially higher than that of Ag<sub>3</sub>PO<sub>4</sub>@ACB, which facilitated the complete utilization of visible light by N,S-Ag<sub>3</sub>PO<sub>4</sub>@ACB. The direct forbidden bands of Ag<sub>3</sub>PO<sub>4</sub>, Ag<sub>3</sub>PO<sub>4</sub>@ACB, and N,S-Ag<sub>3</sub>PO<sub>4</sub>@ACB were at 2.30, 2.04, and 1.86 eV, respectively (Fig. 6b); thus, the forbidden band of Ag<sub>3</sub>PO<sub>4</sub> gradually decreased with the application of ACB as a carrier and after co-doping with N and S. This phenomenon was also confirmed by the indirect forbidden band shown in Fig. 6c, which displays similar results. The XPS valence band spectrum of N,S-Ag<sub>3</sub>PO<sub>4</sub>@ACB (Fig. 6d) can be converted to valence and conduction bands at the NHE according to Eqs. (1) and (2), as reported by Wang et al.<sup>7</sup>. Thus, the valence band of N,S-Ag<sub>3</sub>PO<sub>4</sub>@ACB is estimated to be 1.35 eV and the conduction band is -0.51 eV. In comparison, the valence and conduction bands of Ag<sub>3</sub>PO<sub>4</sub> in a related study by Wang et al.<sup>9</sup> were found to be 2.61 and 0.31 eV, respectively.

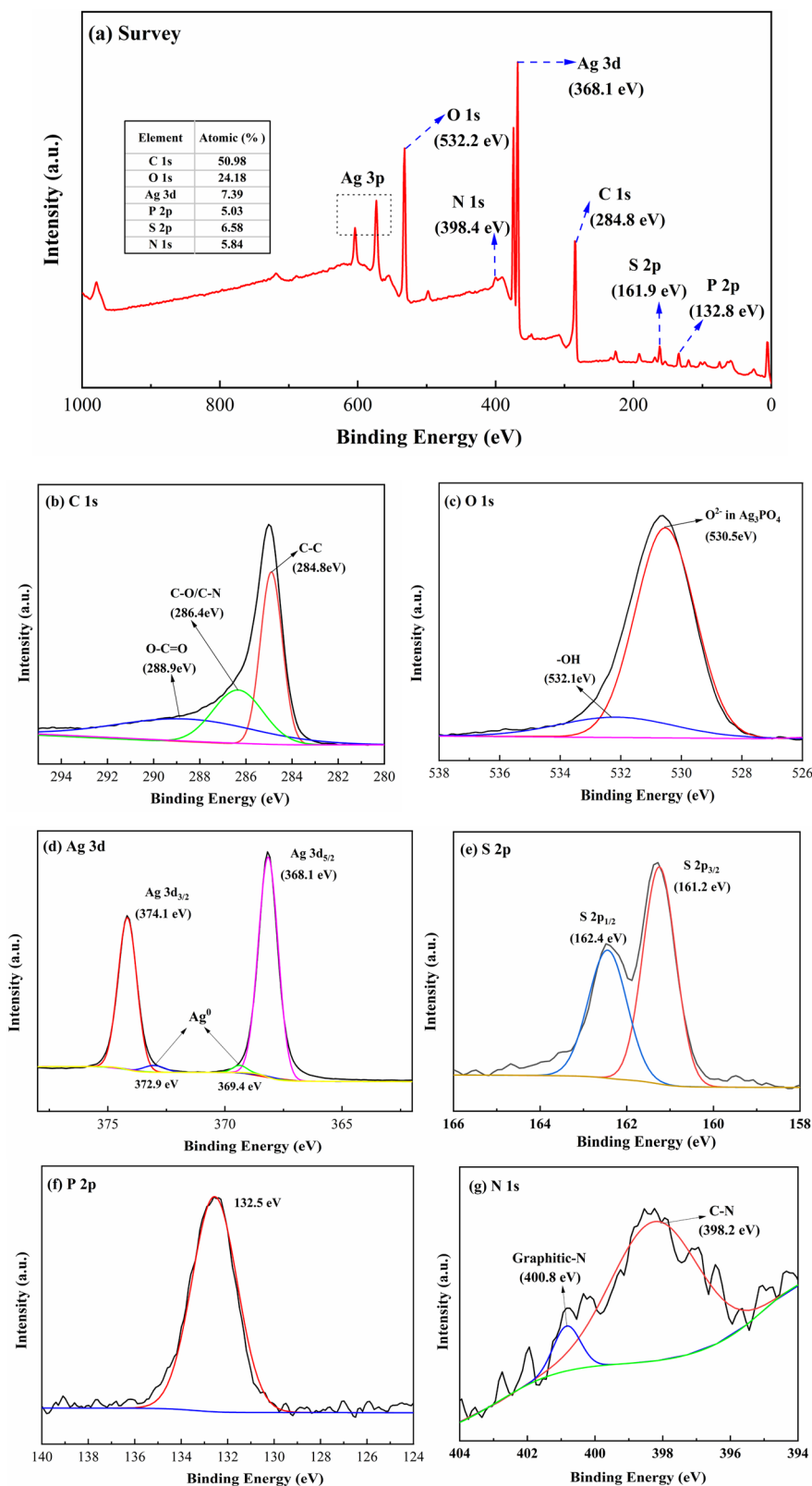
### Adsorption-photocatalytic degradation of NOR performance

The NOR removal performance of the prepared materials was evaluated (Fig. 7). The removal of NOR at an initial concentration of 50 mg L<sup>-1</sup> by N,S-Ag<sub>3</sub>PO<sub>4</sub>@ACB was 90.42% after 120 min of light exposure, compared with 74.17% and 35.45% for the control treatments Ag<sub>3</sub>PO<sub>4</sub>@ACB and pure Ag<sub>3</sub>PO<sub>4</sub>, respectively (Fig. 7a). These results demonstrate that the use of ACB as a carrier promoted the photocatalytic activity of pure Ag<sub>3</sub>PO<sub>4</sub> and that N and S co-doping further enhanced the degradation

efficiency of the Ag<sub>3</sub>PO<sub>4</sub>@ACB composite for NOR. The adsorption effect of ACB on NOR was substantially higher than that of Ag<sub>3</sub>PO<sub>4</sub> because of the influence of the specific surface area. The adsorption-desorption equilibrium of ACB was reached within 60 min in the dark, after which the concentration of NOR decreased insignificantly with increasing irradiation time. Although Ag<sub>3</sub>PO<sub>4</sub> exhibited limited adsorption of NOR in the dark, it could continuously photodegrade NOR after 120 min of irradiation. Consequently, the final NOR removal rate by Ag<sub>3</sub>PO<sub>4</sub> was higher than that by ACB. This result also indicates that the removal of NOR by ACB proceeds mainly via physical adsorption, and the removal by Ag<sub>3</sub>PO<sub>4</sub> proceeds mainly via photocatalytic degradation. The removal mechanisms of NOR by N,S-Ag<sub>3</sub>PO<sub>4</sub>@ACB and Ag<sub>3</sub>PO<sub>4</sub>@ACB included adsorption and photocatalysis; however, photocatalysis was dominant, judging from the combination of removal rate and reaction time.

Figure 7b displays the pseudo-first-order degradation kinetic, and this degradation rate constant of N,S-Ag<sub>3</sub>PO<sub>4</sub>@ACB was 0.0175 min<sup>-1</sup> at 90 min of irradiation, which is 1.73 times higher than that of Ag<sub>3</sub>PO<sub>4</sub>@ACB (0.0101 min<sup>-1</sup>) and 5 times higher than that of Ag<sub>3</sub>PO<sub>4</sub> (0.0035 min<sup>-1</sup>). This implies that N,S-Ag<sub>3</sub>PO<sub>4</sub>@ACB exhibited the strongest visible-light photocatalytic activity, and the N, S-co-doped composite design significantly enhanced the photocatalytic performance compared to Ag<sub>3</sub>PO<sub>4</sub>@ACB and pure Ag<sub>3</sub>PO<sub>4</sub>. However, in terms of the increased rate of pseudo-first-order kinetic degradation, the complexation of ACB as a carrier with Ag<sub>3</sub>PO<sub>4</sub> was superior to N and S co-doping. Additionally, the total organic carbon (TOC) removal rate can demonstrate the mineralization ability of NOR and reflect the photodegradation performance. The TOC removal rate of N,S-Ag<sub>3</sub>PO<sub>4</sub>@ACB after 120 min

**Fig. 5 | XPS spectra of N,S-Ag<sub>3</sub>PO<sub>4</sub>@ACB.**  
 a Survey, b C 1s, c O 1s, d Ag 3d, e S 2p, f P 2p, and g N 1s.



of irradiation was 69.67%, whereas those of Ag<sub>3</sub>PO<sub>4</sub>@ACB and Ag<sub>3</sub>PO<sub>4</sub> were 53.72% and 36.55%, respectively (Fig. 7c). N,S-Ag<sub>3</sub>PO<sub>4</sub>@ACB displayed the highest TOC removal rate, which implied that N,S-Ag<sub>3</sub>PO<sub>4</sub>@ACB degraded NOR more completely and produced more degradation intermediates than Ag<sub>3</sub>PO<sub>4</sub>@ACB and Ag<sub>3</sub>PO<sub>4</sub> over the same period.

### Effects of environmental factors

Generally, environmental factors may affect the photocatalytic activity. As shown in Fig. 8a, the removal rate of N,S-Ag<sub>3</sub>PO<sub>4</sub>@ACB gradually decreased as the initial concentration of NOR was increased from 20 to 60 mg L<sup>-1</sup>, and the rate of decrease also decreased. When the NOR concentration was 20 mg L<sup>-1</sup>, it was evident that N,S-Ag<sub>3</sub>PO<sub>4</sub>@ACB was almost

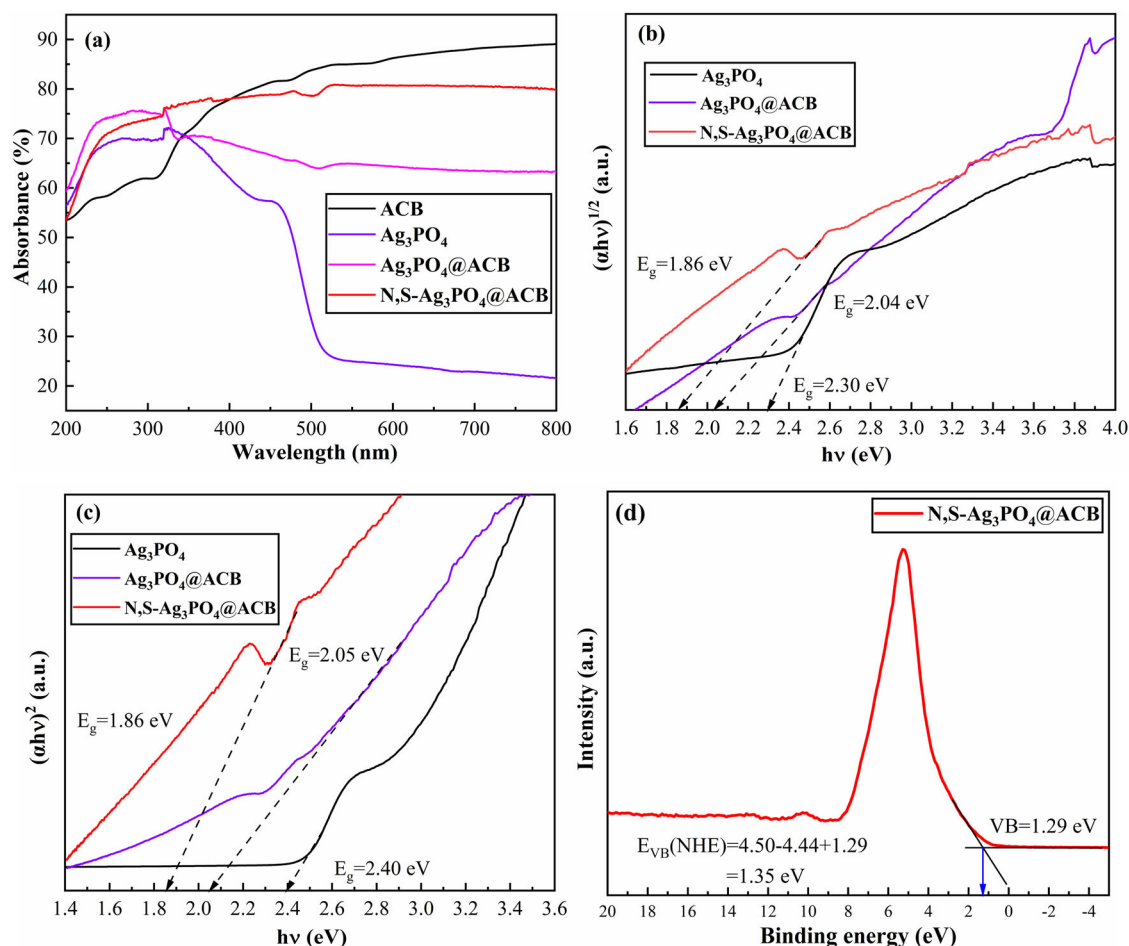


**Fig. 6** | UV-vis/DRS spectra of prepared photocatalysts. **a** UV-vis/DRS spectra, **b** direct band gap based on Tauc plot, **c** indirect band gap based on Tauc plot, and **d** XPS valence band of N,S-Ag<sub>3</sub>PO<sub>4</sub>@ACB.

completely degraded within 60 min of irradiation. When the NOR concentration was increased to 30 mg L<sup>-1</sup>, the time for complete degradation increased to 90 min. This was mainly related to the probability of interfacial contact between the solute composite and the reduction in effective composite active sites. High NOR concentrations (e.g., 60 mg L<sup>-1</sup>) inhibited photogenerated carrier transfer and decreased the photocatalytic degradation rate. The removal rate of NOR by N,S-Ag<sub>3</sub>PO<sub>4</sub>@ACB decreased in the following order: pH = 6.88 > pH = 8.87 > pH = 11.03 > pH = 4.91 > pH = 2.93 (Fig. 8b). This result suggests that the degradation of NOR by N,S-Ag<sub>3</sub>PO<sub>4</sub>@ACB is best in neutral environments, and that both acidic and alkaline environments inhibit it, even though acidic environments inhibit the degradation of NOR more than alkaline environments. Additionally, the degradation rate of NOR by N,S-Ag<sub>3</sub>PO<sub>4</sub>@ACB was reduced by 4.72% in an alkaline environment (pH = 11.03) compared to that at pH = 6.88, whereas it was reduced by 14.50% in an acidic environment (pH = 2.93). This implies that N,S-Ag<sub>3</sub>PO<sub>4</sub>@ACB may be buffered in alkaline environments and has little impact on the photocatalytic degradation of NOR. However, strongly acidic environments have a significant impact, which is related to the protonation of NOR and electrostatic repulsion at the nonhomogeneous interface<sup>25</sup>.

As shown in Fig. 8c, the NOR degradation rate by N,S-Ag<sub>3</sub>PO<sub>4</sub>@ACB gradually increased with increasing dosage. When the dosage was 2 g L<sup>-1</sup>, NOR was almost completely removed by irradiation for ~90 min. This is related to the larger S<sub>BET</sub> and surface-active sites of N,S-Ag<sub>3</sub>PO<sub>4</sub>@ACB; the higher dosage of the photocatalyst significantly enhanced the adsorption of NOR and promoted the rapid transfer of degradation intermediates on the surface of N,S-Ag<sub>3</sub>PO<sub>4</sub>@ACB. The effect of the coexisting ions on NOR degradation is shown in Fig. 8d. Overall, NaCl and NaNO<sub>3</sub> treatments had

little impact on the degradation of NOR; however, Na<sub>2</sub>SO<sub>4</sub> and Na<sub>2</sub>CO<sub>3</sub> treatments significantly reduced the degradation rate of NOR. Moreover, in the dark, there was little impact on the adsorption of NOR by N,S-Ag<sub>3</sub>PO<sub>4</sub>@ACB because of the low concentrations of these coexisting ions. The differences between the four different coexisting ions were mainly related to the charges carried by the coexisting ions, the molecular weight size, the crystal size of the salt ions, and the solution pH. Na<sub>2</sub>CO<sub>3</sub> exhibited the strongest reduction of 16.97% owing to the alkaline nature of this treatment in solution.

### Reusability and photostability

Based on the above typical adsorption-photocatalytic degradation experiments, five rounds of recycling tests were conducted to study the reusability and photostability of N,S-Ag<sub>3</sub>PO<sub>4</sub>@ACB. The degradation rate of NOR by N,S-Ag<sub>3</sub>PO<sub>4</sub>@ACB decreased by 10.08% relative to the first cycle after five recycling tests (in Fig. 9a). This implied that the recyclability of N,S-Ag<sub>3</sub>PO<sub>4</sub>@ACB was moderate. To further investigate the photostability of N,S-Ag<sub>3</sub>PO<sub>4</sub>@ACB, the samples were centrifuged after five recycling tests and then washed with ultrapure water, and the recovered N,S-Ag<sub>3</sub>PO<sub>4</sub>@ACB were dried at 80 °C for 10 h before testing. XRD patterns and FTIR spectra were obtained of the recovered samples. As shown in Fig. 9b, the XRD results indicate that the crystal structure of N,S-Ag<sub>3</sub>PO<sub>4</sub>@ACB was not significantly altered, except for the extra impurity peak at 2θ = 19.4° which is not matched to the crystal. The FTIR results (Fig. 9c) indicate a slight increase in the intensity of the -OH broad stretching vibrational peak at 3420 cm<sup>-1</sup> after the recycling tests, which may be related to the adsorption of degradation intermediates containing -OH functional groups. The positions and characteristic peak intensities of the other surface functional

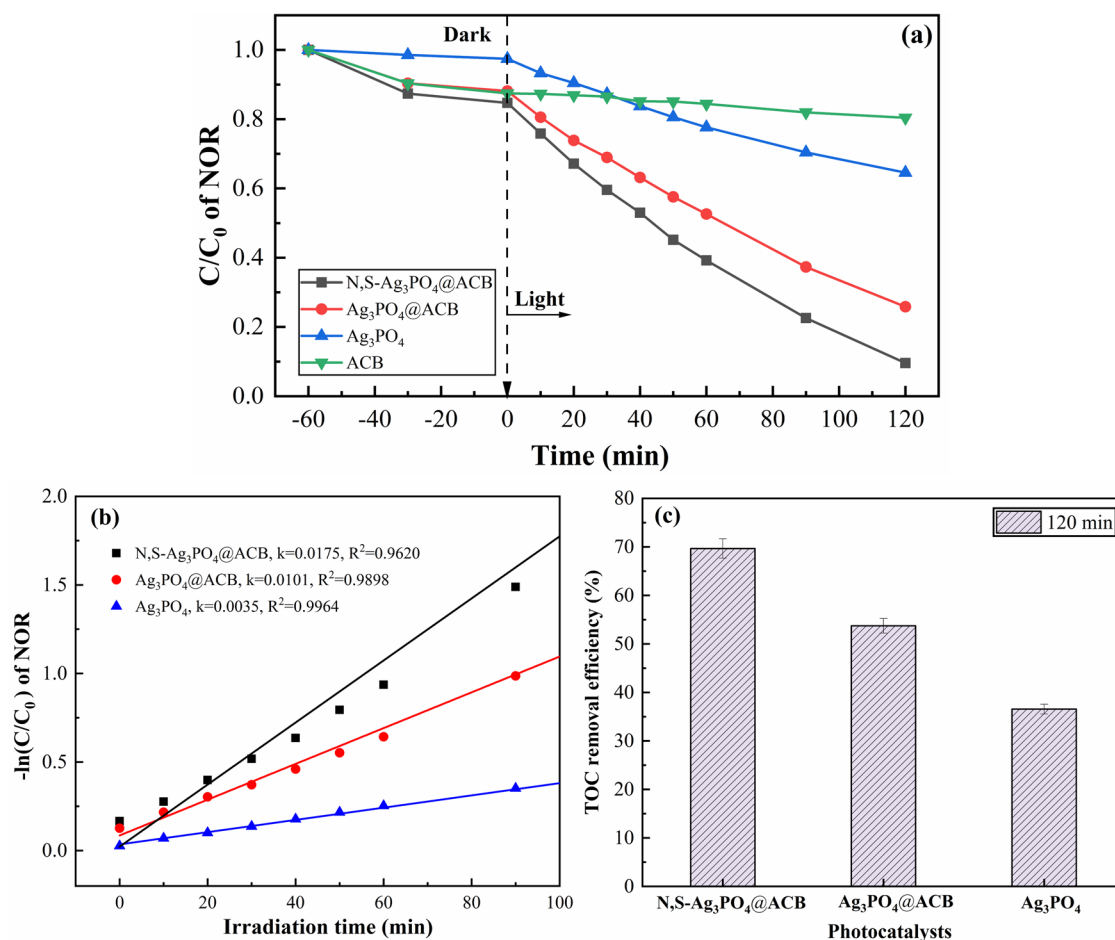


**Fig. 7 | Adsorption-photocatalytic degradation performance analysis.**

**a** Adsorption-photocatalytic degradation of NOR using the prepared photocatalysts. **b** Pseudo-first-order kinetic curves of NOR by the prepared photocatalysts. **c** TOC

removal efficiency. (Experimental conditions: initial concentrations of NOR at  $50 \text{ mg L}^{-1}$ , photocatalysts dosage of  $1 \text{ g L}^{-1}$ , initial pH of  $\sim 7.0$ , 500 W xenon lamp).

groups of N,S-Ag<sub>3</sub>PO<sub>4</sub>@ACB did not change significantly, indicating that the N, S-co-doped biochar-based composites had better photostability.

### Actual wastewater treatment

The degradation of NOR in wastewater 1# (from the rabbit plant) and wastewater 2# (from the chicken plant) by N,S-Ag<sub>3</sub>PO<sub>4</sub>@ACB was 71.80% and 82.88%, respectively, after 180 min of irradiation (Fig. 9d). Additionally, these industrial wastewaters contain interfering ions (Supplementary Table 2). However, the satisfactory degradation of N,S-Ag<sub>3</sub>PO<sub>4</sub>@ACB in NOR-containing wastewater suggests that this composite photocatalyst has the potential to treat highly concentrated wastewater.

### Photogenerated carrier behavior

The photoresponsivity and photocurrent density of N,S-Ag<sub>3</sub>PO<sub>4</sub>@ACB were considerably higher than those of Ag<sub>3</sub>PO<sub>4</sub>@ACB and pure Ag<sub>3</sub>PO<sub>4</sub> (Fig. 10a). The photocurrent density of N,S-Ag<sub>3</sub>PO<sub>4</sub>@ACB increased with increasing irradiation time. However, as the light exposure time increased, the photocurrent density of pure Ag<sub>3</sub>PO<sub>4</sub> remained constant, whereas that of Ag<sub>3</sub>PO<sub>4</sub>@ACB decreased slightly. This implies that the separation efficiency of N,S-Ag<sub>3</sub>PO<sub>4</sub>@ACB for photogenerated electron-hole pairs is superior to that of Ag<sub>3</sub>PO<sub>4</sub>@ACB and Ag<sub>3</sub>PO<sub>4</sub>, which is mainly attributed to N and S co-doping to construct the Ag<sub>2</sub>S/Ag<sub>3</sub>PO<sub>4</sub>/ACB heterojunction, and that N enhances the electrical conductivity and defect degree of the composite. EIS Nyquist plots are shown in Fig. 10b, where N,S-Ag<sub>3</sub>PO<sub>4</sub>@ACB possesses a smaller Nyquist radius, implying that N,S-Ag<sub>3</sub>PO<sub>4</sub>@ACB has a

lower charge transfer resistance and higher charge transfer efficiency than those of Ag<sub>3</sub>PO<sub>4</sub>@ACB and Ag<sub>3</sub>PO<sub>4</sub>. This suggests that N,S-Ag<sub>3</sub>PO<sub>4</sub>@ACB effectively prevented photogenerated carrier separation<sup>20</sup>. In addition, the introduction of ACB enhances the charge transfer of Ag<sub>3</sub>PO<sub>4</sub><sup>9</sup>. Figure 10c shows that Ag<sub>3</sub>PO<sub>4</sub> produced a strong steady-state photoluminescence (PL) spectrum near 550 nm. Tian et al.<sup>28</sup> demonstrated that the strong emission peak of Ag<sub>3</sub>PO<sub>4</sub> is near 550 nm, indicating that the photon energy is approximately equal to its forbidden band energy ( $\sim 2.4 \text{ eV}$ ), and is therefore considered to be a recombination of photogenerated electrons and holes derived from Ag<sub>3</sub>PO<sub>4</sub>. However, the spectra of N,S-Ag<sub>3</sub>PO<sub>4</sub>@ACB and Ag<sub>3</sub>PO<sub>4</sub>@ACB exhibited significant blue shifts. This is mainly due to the introduction of ACB and the co-doping of N and S, suggesting that there is an intrinsic potential in the direction from Ag<sub>3</sub>PO<sub>4</sub> to ACB and that strong interactions may lead to a redistribution of the interfacial charge density, that is, the electrons move from Ag<sub>3</sub>PO<sub>4</sub> to ACB<sup>34</sup>. In summary, the electrochemical analysis and PL spectra confirmed that N,S-Ag<sub>3</sub>PO<sub>4</sub>@ACB possessed good photogenerated charge separation efficiency.

### Roles of reactive species

Furthermore, the active species were identified to determine the reasons for the excellent performance of N,S-Ag<sub>3</sub>PO<sub>4</sub>@ACB, and the role of the dominant free radicals in the synergistic enhancement of photocatalysis. Figure 11a shows that N,S-Ag<sub>3</sub>PO<sub>4</sub>@ACB degraded 90.42% of NOR without scavenger. When the addition of a scavenger reduced the degradation to 41.08%, 45.53%, 46.24%, and 87.45% in the BQ (corresponding to  $\cdot\text{O}_2^-$ ), AO ( $\text{H}^+$ ), TBA ( $\cdot\text{OH}$ ), and MA ( $\text{e}^-$ ) treatments, respectively. This also implies

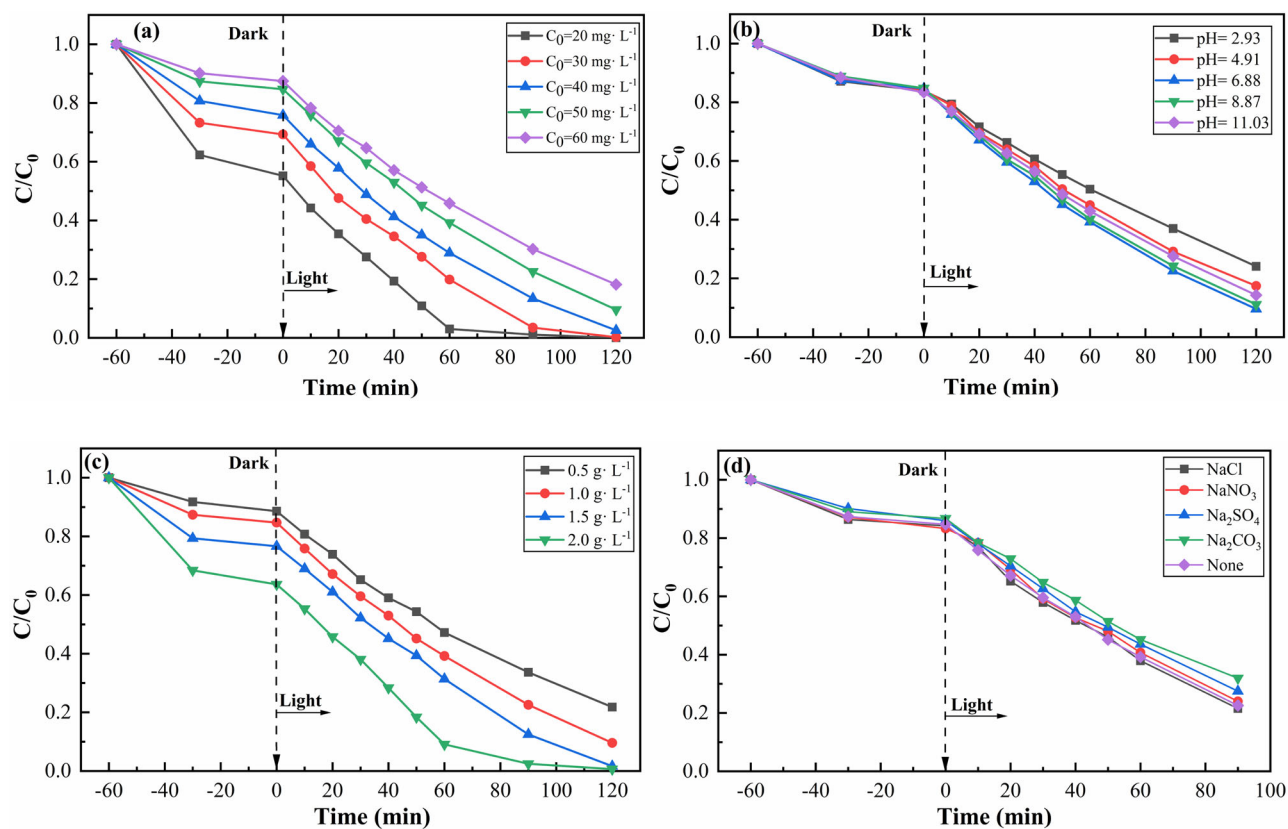


**Fig. 8** | Effects of different factors on the adsorption-degradation of NOR using N,S-Ag<sub>3</sub>PO<sub>4</sub>@ACB. **a** initial concentration, **b** initial pH, **c** addition dosage, and **d** coexisting ions. (Except for the investigated parameter, other parameters were

fixed: initial concentration of 50 mg L<sup>-1</sup>, addition dosage of 1 g L<sup>-1</sup>, initial pH of ~7.0, 500 W xenon lamp, no coexisting ions).

that  $\cdot\text{O}_2^-$ ,  $\text{H}^+$ , and  $\cdot\text{OH}$  play a dominant role in this photocatalytic system. Additionally, the conduction band of N,S-Ag<sub>3</sub>PO<sub>4</sub>@ACB is located at  $-0.51$  eV, which is more negative than the  $\text{O}_2/\text{O}_2^-$  oxidation potential ( $-0.33$  eV), which favors the system to produce more  $\cdot\text{O}_2^-$ . The valence band of N,S-Ag<sub>3</sub>PO<sub>4</sub>@ACB is located at  $1.35$  eV, which is lower than the  $\text{OH}^-/\cdot\text{OH}$  oxidation potential ( $+2.40$  eV); this does not favor the generation of  $\cdot\text{OH}$ . However, the surface of ACB contains several EPFRs, which could induce the generation of  $\cdot\text{OH}$ <sup>35</sup>.

To further verify this result, ESR was measured. No obvious 5,5-dimethyl-1-pyrroline N-oxide (DMPO)- $\cdot\text{OH}$  (fourfold peaks) and DMPO- $\cdot\text{O}_2^-$  (sixfold peaks) signals were detected for N,S-Ag<sub>3</sub>PO<sub>4</sub>@ACB in the dark (Fig. 11b, c). However, after 10 min of irradiation, typical DMPO- $\cdot\text{O}_2^-$  and DMPO- $\cdot\text{OH}$  signals were observed, which indicates that N,S-Ag<sub>3</sub>PO<sub>4</sub>@ACB was able to produce  $\cdot\text{OH}$  and  $\cdot\text{O}_2^-$  radicals under visible-light irradiation. This result is consistent with those of the free-radical trapping experiments, suggesting that  $\cdot\text{OH}$  and  $\cdot\text{O}_2^-$  radicals play an important role in the degradation of NOR by N,S-Ag<sub>3</sub>PO<sub>4</sub>@ACB. Additionally, the co-doping of N, S could significantly enhance the DMPO- $\cdot\text{OH}$  signals of Ag<sub>3</sub>PO<sub>4</sub>@ACB (Fig. 11b, c), which is closely related to the defects and energy band structure of N,S-Ag<sub>3</sub>PO<sub>4</sub>@ACB. Moreover, the use of ACB as a carrier increased the intensity of the DMPO- $\cdot\text{OH}$  signals of Ag<sub>3</sub>PO<sub>4</sub>, which may be attributed to the abundant EPFRs on the ACB surface<sup>35</sup>.

### Synergistic mechanisms

Considering the above results, it could be inferred that the degradation mechanisms of NOR by N,S-Ag<sub>3</sub>PO<sub>4</sub>@ACB generally included three parts. First, NOR was adsorbed onto the surface of N,S-Ag<sub>3</sub>PO<sub>4</sub>@ACB by physisorption and chemisorption, and related adsorption mechanisms have been reported previously<sup>9,30</sup>. Second, a non-homogeneous photocatalysis takes place at the interfaces between N,S-Ag<sub>3</sub>PO<sub>4</sub>@ACB and NOR to

generate ROS, which gradually degrade NOR<sup>23</sup>. Finally, the degradation intermediates detach from the surface of N,S-Ag<sub>3</sub>PO<sub>4</sub>@ACB, thus releasing the active sites, which reabsorb the NOR and the degraded macromolecular intermediates to continue photocatalysis. The ROS generated during photocatalysis are strongly oxidized until NOR is gradually mineralized to H<sub>2</sub>O and CO<sub>2</sub><sup>7</sup>.

The paths of the possible photogenerated carriers for N,S-Ag<sub>3</sub>PO<sub>4</sub>@ACB are illustrated in Fig. 12. According to Tian et al.<sup>28</sup> and Shi et al.<sup>33</sup> the conduction band ( $-0.025$  eV) and valence band ( $0.0965$  eV) of Ag<sub>2</sub>S were estimated to have larger negative potentials than the conduction band ( $0.31$  eV) and valence band ( $2.61$  eV) of Ag<sub>3</sub>PO<sub>4</sub>, respectively. Under visible light irradiation, both Ag<sub>2</sub>S and Ag<sub>3</sub>PO<sub>4</sub> can be excited to produce photogenerated electrons and holes in their conduction and valence bands, respectively. For the double silver composite system, a small amount of Ag was inevitably produced under visible-light irradiation, as demonstrated in the XRD patterns (Fig. 2a) and XPS analyses (Fig. 5). The surface plasmon resonance (SPR) effect of the Ag nanoparticles enhances the photocatalytic efficiency of Ag<sub>3</sub>PO<sub>4</sub><sup>31</sup>. Moreover, the Fermi energy level of Ag is more negative than that of Ag<sub>3</sub>PO<sub>4</sub>, which facilitates the transport of photogenerated charges between Ag<sub>2</sub>S and Ag<sub>3</sub>PO<sub>4</sub>. Ag nanoparticles act as photogenerated carrier-binding sites with ACB during photocatalysis, resulting in the rapid combination of holes generated by photoexcitation near the valence band of Ag<sub>2</sub>S and photogenerated electrons near the conduction band of Ag<sub>3</sub>PO<sub>4</sub><sup>36</sup>. Therefore, in this composite system, the photocatalytic mechanism of the Z-scheme was more compatible. Additionally, a conventional Type-II heterojunction would not be favorable for the formation of  $\cdot\text{O}_2^-$  radicals, which contradicts the results of the free radical trapping experiments described above. Shi et al.<sup>33</sup> concluded that the oxidation potential of  $\text{H}^+$  in the valence band of Ag<sub>2</sub>S is too weak to degrade organic pollutants and that the conduction band potential of Ag<sub>3</sub>PO<sub>4</sub> is

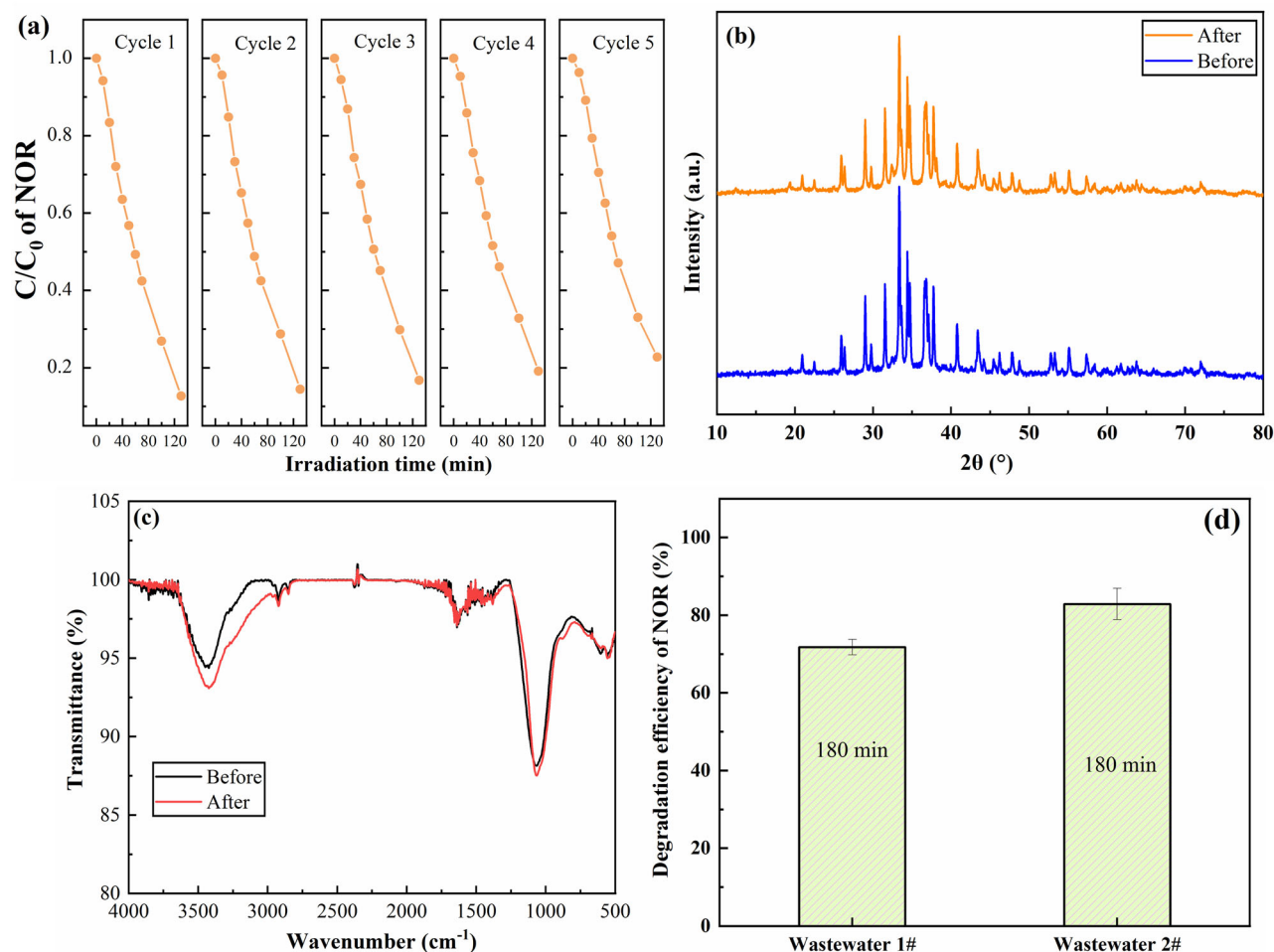


**Fig. 9 | Reusability, photostability and wastewater treatment performance analysis.** **a** Recycling performance tests of photocatalytic degradation for NOR removal using N,S-Ag<sub>3</sub>PO<sub>4</sub>@ACB. (Experimental conditions: initial concentration of 50 mg L<sup>-1</sup>, addition dosage of 1 g L<sup>-1</sup>, initial pH of ~7.0, 500 W xenon lamp). **b** The XRD patterns of N,S-Ag<sub>3</sub>PO<sub>4</sub>@ACB before and after the recycling tests. **c** The FTIR

spectroscopy of N,S-Ag<sub>3</sub>PO<sub>4</sub>@ACB before and after the recycling tests. **d** Actual wastewater tests for NOR removal using N,S-Ag<sub>3</sub>PO<sub>4</sub>@ACB. (Experimental conditions: addition dosage of 1 g L<sup>-1</sup>, 500 W xenon lamp, no adjustment of other parameters).

more positive than the O<sub>2</sub>/·O<sub>2</sub><sup>-</sup> oxidation potential. Therefore, the e<sup>-</sup> accumulated in the conduction band of Ag<sub>3</sub>PO<sub>4</sub> may not be able to generate ·O<sub>2</sub><sup>-</sup> radicals via adsorbed dissolved oxygen. These typical Z-scheme heterojunctions (Fig. 12) promote the photocatalytic activity of N,S-Ag<sub>3</sub>PO<sub>4</sub>@ACB over Ag<sub>3</sub>PO<sub>4</sub>@ACB.

Furthermore, the mechanisms of enhanced photocatalysis by synergistic N and S co-doping of biochar may include the following possible contributions. (1) Liu et al.<sup>30</sup> suggested that the functional group density on the surface of metal- and heteroatom-doped biochar-based composites increases owing to the presence of N- and S-containing groups. This implies that N,S-Ag<sub>3</sub>PO<sub>4</sub>@ACB has improved affinity for pollutants and better adsorption properties than Ag<sub>3</sub>PO<sub>4</sub>@ACB. This is corroborated by the surface properties shown in Table 1, where N and S co-doping increased the specific surface area of N,S-Ag<sub>3</sub>PO<sub>4</sub>@ACB, increased its pore volume, and reduced its average pore size. Moreover, in the N,S-Ag<sub>3</sub>PO<sub>4</sub>@ACB system, the lone pairs of electrons in N and S may act as electron donors. Specifically, the electronegativity of N (3.04) is higher than that of C (2.54), which may modify the electron transfer and affect the electron spin properties of biochar<sup>27</sup>. Additionally, N,S-Ag<sub>3</sub>PO<sub>4</sub>@ACB contains graphitic N (Fig. 5), which is considered the most favorable for the activation because the nonuniform distribution of graphitic N in the hexagon tends to cleave or dissociate the individual chemical bonds of the pollutants during their interaction with N,S-Ag<sub>3</sub>PO<sub>4</sub>@ACB<sup>30</sup>. The electronegativity of S (2.58) is close to that of the carbon atom, which could induce a spin charge in the

carbon lattice of the biochar, creating more catalytic centers for N,S-Ag<sub>3</sub>PO<sub>4</sub>@ACB<sup>27</sup>. Moreover, Liu et al.<sup>30</sup> reviewed many related reports and found that S-containing composites facilitated interfacial electron transfer between the photocatalyst and metal atoms because S could easily oxidize to S<sup>2-</sup>. (2) The surface porosity, defect structure, and OFGs of biochar are potential active sites<sup>14</sup>, which are enhanced during both the adsorption stage and the desorption-diffusion of degradation intermediates<sup>16,17</sup>. In addition, the high electrical conductivity of ACB promotes the transfer of photo-generated electrons<sup>7,14</sup>. Previous studies have also found that biochar surfaces contain many EPFRs that boost ROS generation in composites<sup>13</sup>. (3) Ag<sub>3</sub>PO<sub>4</sub> is an n-type semiconductor<sup>37</sup>, whereas Ag<sub>2</sub>S is a p-type semiconductor; thus, a p-n heterojunction may be formed between them, which enhances the effective separation of photogenerated carriers<sup>38</sup>. Furthermore, Meng et al.<sup>39</sup> proposed the concept of a photocatalytic relative p-n heterojunction; N,S-Ag<sub>3</sub>PO<sub>4</sub>@ACB may behave similarly, as well as being the Z-scheme transfer type of the p-n heterojunction, which reveals that the noble metal Ag loading and non-metallic N, S co-doping provided endogenous dynamics for photogenerated carrier migration.

#### Degradation process and pathways of NOR

Figure 13 shows the 3D EEMs spectra of the residual NOR solutions collected at different times. As shown in Fig. 13a, the initial NOR solution before irradiation exhibited a strong fluorescence characteristic peak at Ex/Em = 200–360/370–530 nm. This is significantly different from that

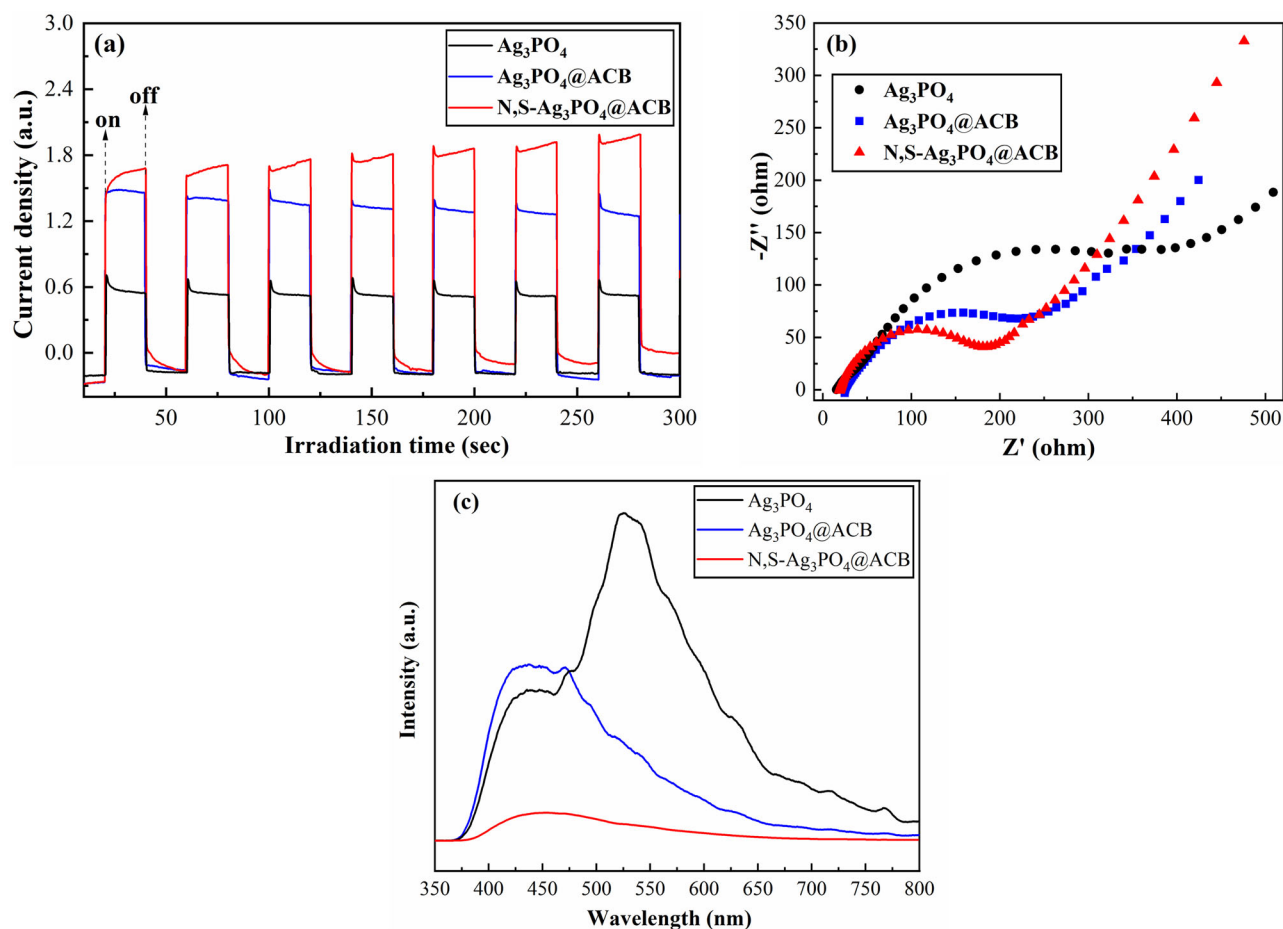


**Fig. 10 | Electrochemical analysis and photoluminescence spectroscopy of the prepared photocatalysts. a** Transient photocurrent responses, **b** EIS Nyquist profiles, and **c** PL spectra.

reported by Liang et al.<sup>29</sup> in which the original NOR exhibited two excitation/emission regions at  $E_x/E_m = 250\text{--}300/425\text{--}475$  nm and  $E_x/E_m = 300\text{--}350/425\text{--}475$  nm. The higher concentration of NOR ( $50\text{ mg L}^{-1}$ ) used in this study caused these two peaks to merge. NOR generates a strong fluorescent signal related to its molecular structure, and the excitation/emission region depends on the concentration of humic acid<sup>29</sup>. After 10 min of irradiation, the center of this large fluorescence peak was slightly red-shifted along the emission axis, which could be a humic acid-like substance produced by NOR photodegradation. As the photocatalytic reaction proceeded (Fig. 13b–d), this large fluorescence peak gradually divided into two smaller fluorescence peak; the peaks flattened and their intensities gradually decreased. Additionally, the center of this large fluorescence peak gradually blue-shifted along the emission axis, which may be attributed to the disruption of the conjugated heterocyclic structure of NOR, decomposition of NOR into small-molecule organics, and cleavage of specific functional groups in the degradation process. At 120 min of irradiation (Fig. 13e), the intensities of these two fluorescence peaks decreased significantly, indicating that the NOR molecules were photocatalytically degraded, and the concentration gradually decreased with further mineralization of the degradation intermediates. Thus, the 3D EEMs results showed that NOR molecules may be progressively degraded via N,S- $\text{Ag}_3\text{PO}_4$ @ACB visible-light photocatalysis until complete removal.

The possible photocatalytic degradation intermediates of NOR by N,S- $\text{Ag}_3\text{PO}_4$ @ACB were identified using HPLC-MS. Detailed mass spectra are shown in Supplementary Fig. 2, and the deduced intermediate degradation products are presented in Supplementary Table 3. Based on the data for the degradation intermediates and the results of the 3D EEMs analysis, possible degradation pathways for NOR were proposed, as illustrated in Fig. 14.

Pathway I involved photocatalysis by the NOR transformation mechanism of substituted F atoms, quinolone group transformation, and piperazine ring cleavage. First, the  $\cdot\text{OH}$  generated via photocatalytic degradation replaced the F atoms in the NOR, converting NOR to P1 ( $m/z = 318$ ). Subsequently, the continued addition of two hydroxyl groups to the C atom in the NOR-unsaturated bond preferentially produced P2 ( $m/z = 352$ ), whereas P3 ( $m/z = 323$ ) was produced by loss of the  $-\text{HCO}$  bond. Similar degradation pathways have been reported by Chen and Chu<sup>40</sup> and Shah et al.<sup>41</sup> in which NOR directly formed P1 and P3 by replacing F and losing the  $-\text{C}=\text{O}$  bond<sup>42</sup>. Next, P3 was converted to P4 ( $m/z = 277$ ) by the loss of the  $-\text{HCOOH}$  bond, which was then converted to P5 ( $m/z = 251$ ) by cleavage of the piperazine ring and loss of the  $-\text{C}_2\text{H}_2$  bond. P5 extracted electrons from N, and the C–N bond was cleaved, followed by the loss of the ethylenediamine group ( $-\text{NH}_2\text{--CH}_2\text{--CH}_2\text{--NH}_2$  chain), which in turn was converted to P6 ( $m/z = 192$ ). Finally, owing to the continuous attack of ROS on the C atom, NOR and some of the intermediates were converted to P7 ( $m/z = 107$ ) through a series of reactions. In summary, degradation pathway I is associated with the replacement and elimination of F atoms, ring opening, decarboxylation for quinolone group conversion, and possible piperazine ring cleavage through the loss of the ethylenediamine group. As indicated by degradation pathway II, the original NOR was gradually converted to P8 ( $m/z = 296$ ), mainly by decarboxylation and opening of the piperazine ring during photodegradation, after which the alkyl group was removed to produce P11 ( $m/z = 227$ ). Additionally, the unsaturated carbon atom in NOR may also be converted to P9 ( $m/z = 290$ ) by decarboxylation and dehydrogenation reactions, and lose O to form P10 ( $m/z = 276$ ). In summary, degradation path II is associated with decarboxylation and dealkylation. For degradation pathway III, the original NOR was converted

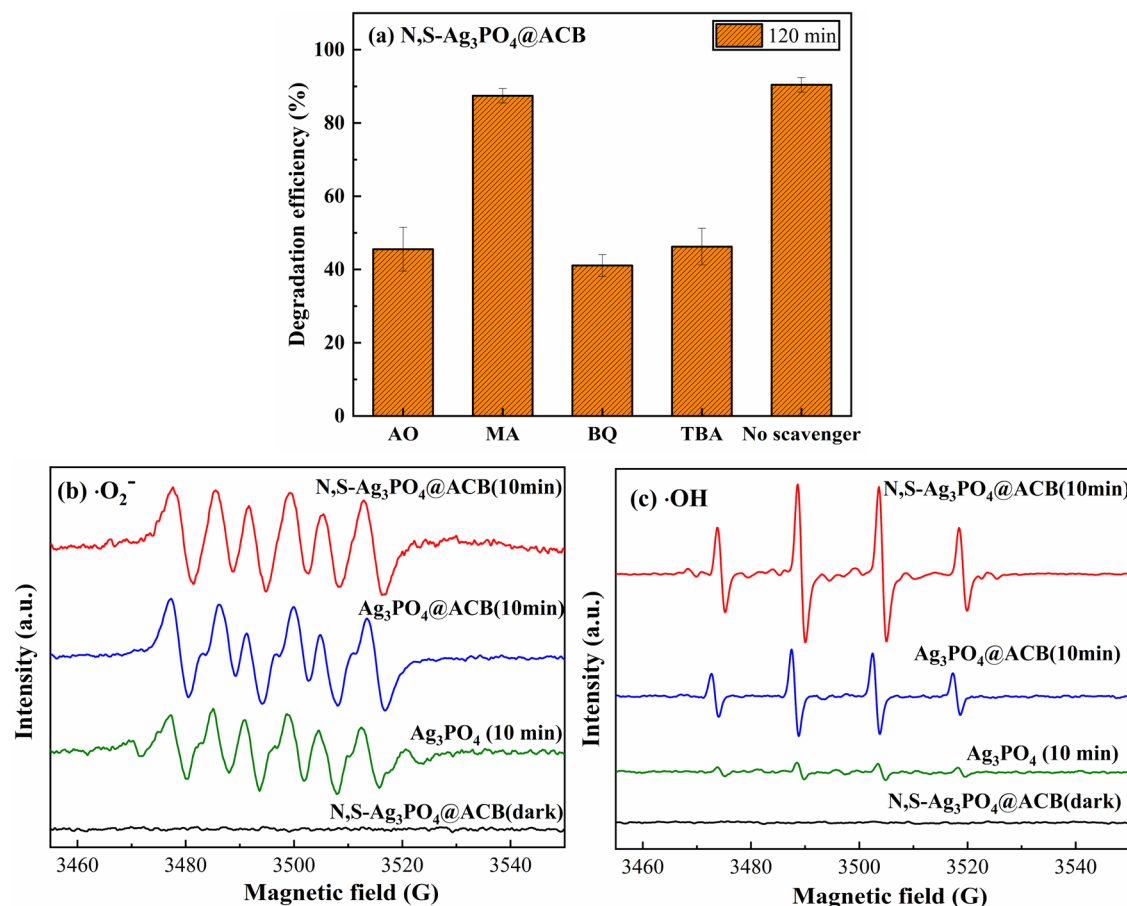


**Fig. 11 | Dominant free radical analysis.** a Active radical species trapping experiments for the photocatalytic degradation of NOR under visible light irradiation, and b, c ESR spectra of radical adducts trapped by DMPO ( $\cdot\text{O}_2^-$  and  $\cdot\text{OH}$ ) in the dark and with the visible light irradiation of 10 min.

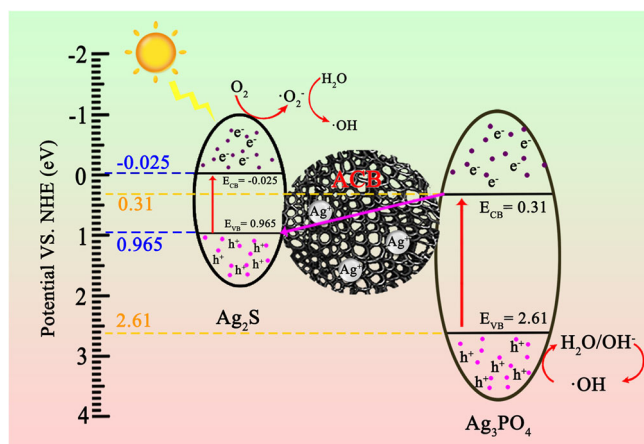


**Fig. 12 | Schematic illustration of photogenerated carrier transport mode in N,S-Ag<sub>3</sub>PO<sub>4</sub>@ACB.**

to P12 ( $m/z = 336$ ) via the addition of hydroxyl groups ( $\cdot\text{OH}$  instead of H) during ROS oxidation which was then converted to P13 ( $m/z = 352$ ) through the replacement of F atoms with hydroxyl groups. This was immediately followed by conversion to P14 ( $m/z = 346$ ) via dehydroxylation, deoxygenation to P15 ( $m/z = 332$ ), opening of the piperazine ring to P16 ( $m/z = 291$ ), and complete removal of the remaining piperazine ring to P23 ( $m/z = 234$ ). Moreover, the degradation intermediate P12 ( $m/z = 336$ ) may also be directly converted to P17 ( $m/z = 350$ ) by opening the piperazine ring under the action of ROS, followed by deoxygenation to produce P18

( $m/z = 322$ ) or P19 ( $m/z = 322$ ), two tautomers. The conversion was continued by deoxygenation to P20 ( $m/z = 294$ ) and deamidation to P21 ( $m/z = 279$ ). Finally, it was converted to P22 ( $m/z = 261$ ) by replacing the F atom and to P23 ( $m/z = 234$ ) by removing the piperazine ring in the presence of ROS. Overall, degradation pathway III involves the oxidative cleavage of the piperazine ring by  $\cdot\text{OH}$  and the replacement of F. This pathway III is supported by Li et al.<sup>6</sup>. Notably, the NOR degradation intermediate P7 ( $m/z = 107$ ) in this study has rarely been found in previous reports.

### Discussion

A novel N,S-Ag<sub>3</sub>PO<sub>4</sub>@ACB composite was prepared via hydrothermal synthesis and chemical co-precipitation. The degradation pathway of NOR and the factors affecting the degradation were investigated, revealing the synergistic enhancement mechanisms of biochar with N and S co-doping. Multiple characterizations showed that N,S-Ag<sub>3</sub>PO<sub>4</sub>@ACB is an Ag<sub>2</sub>S/Ag<sub>3</sub>PO<sub>4</sub>/ACB composite photocatalyst with a Z-scheme p-n heterojunction containing Ag nanoparticles. N, S co-doping further enriched the elemental composition, surface functional groups, and defects of the biochar-based composite, activating its pore structure and increasing its specific surface area (304.00 m<sup>2</sup> g<sup>-1</sup>) and pore volume. N,S-Ag<sub>3</sub>PO<sub>4</sub>@ACB exhibited absorbance from 200 to 800 nm; furthermore, its forbidden band was narrowed (1.86 eV), and its conduction and valence bands were -0.51 and 1.35 eV, respectively. N,S-Ag<sub>3</sub>PO<sub>4</sub>@ACB degraded 90.42% of NOR (50 mg L<sup>-1</sup>) after 120 min of irradiation; this removal rate was significantly higher than that of Ag<sub>3</sub>PO<sub>4</sub>@ACB and Ag<sub>3</sub>PO<sub>4</sub>. The degradation rate constant was 0.0175 min<sup>-1</sup>, which was 1.73 and 5.00 times higher than those of Ag<sub>3</sub>PO<sub>4</sub>@ACB and Ag<sub>3</sub>PO<sub>4</sub>, respectively. N,S-Ag<sub>3</sub>PO<sub>4</sub>@ACB removed 69.67% TOC; this removal rate was 1.29 and 1.91 times higher than those of Ag<sub>3</sub>PO<sub>4</sub>@ACB and Ag<sub>3</sub>PO<sub>4</sub>, respectively. The environmental factors

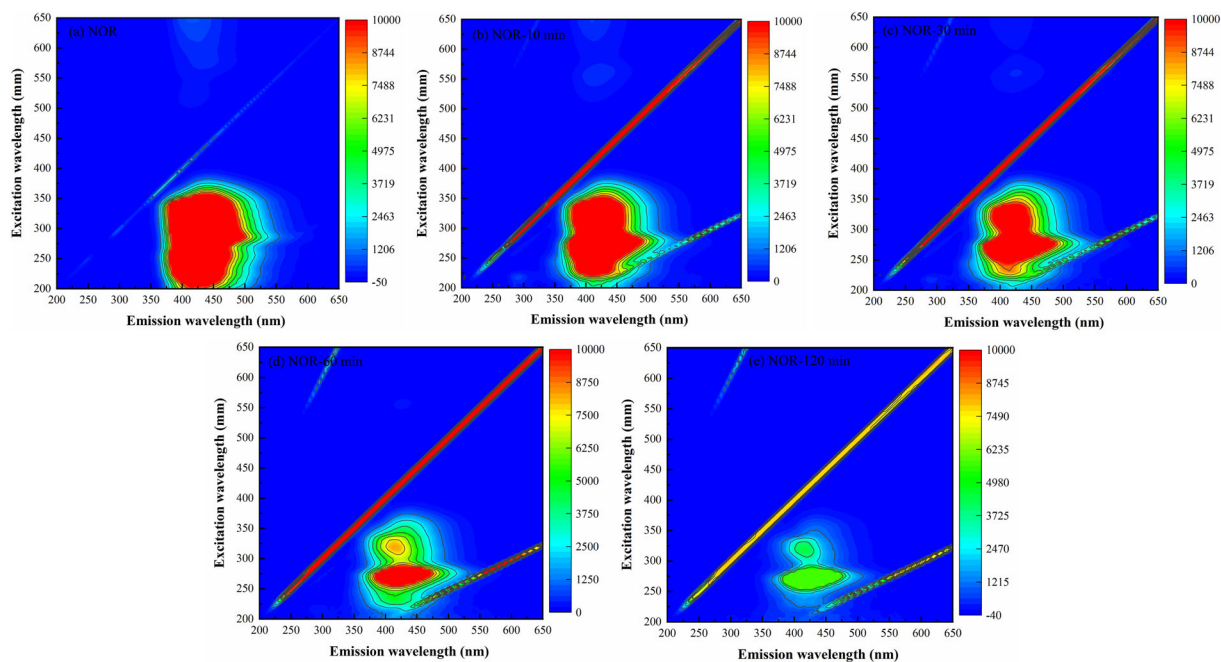


Fig. 13 | Three-dimensional fluorescence of NOR degradation under visible light irradiation. a Original NOR solution, b 10 min, c 30 min, d 60 min, and e 120 min.

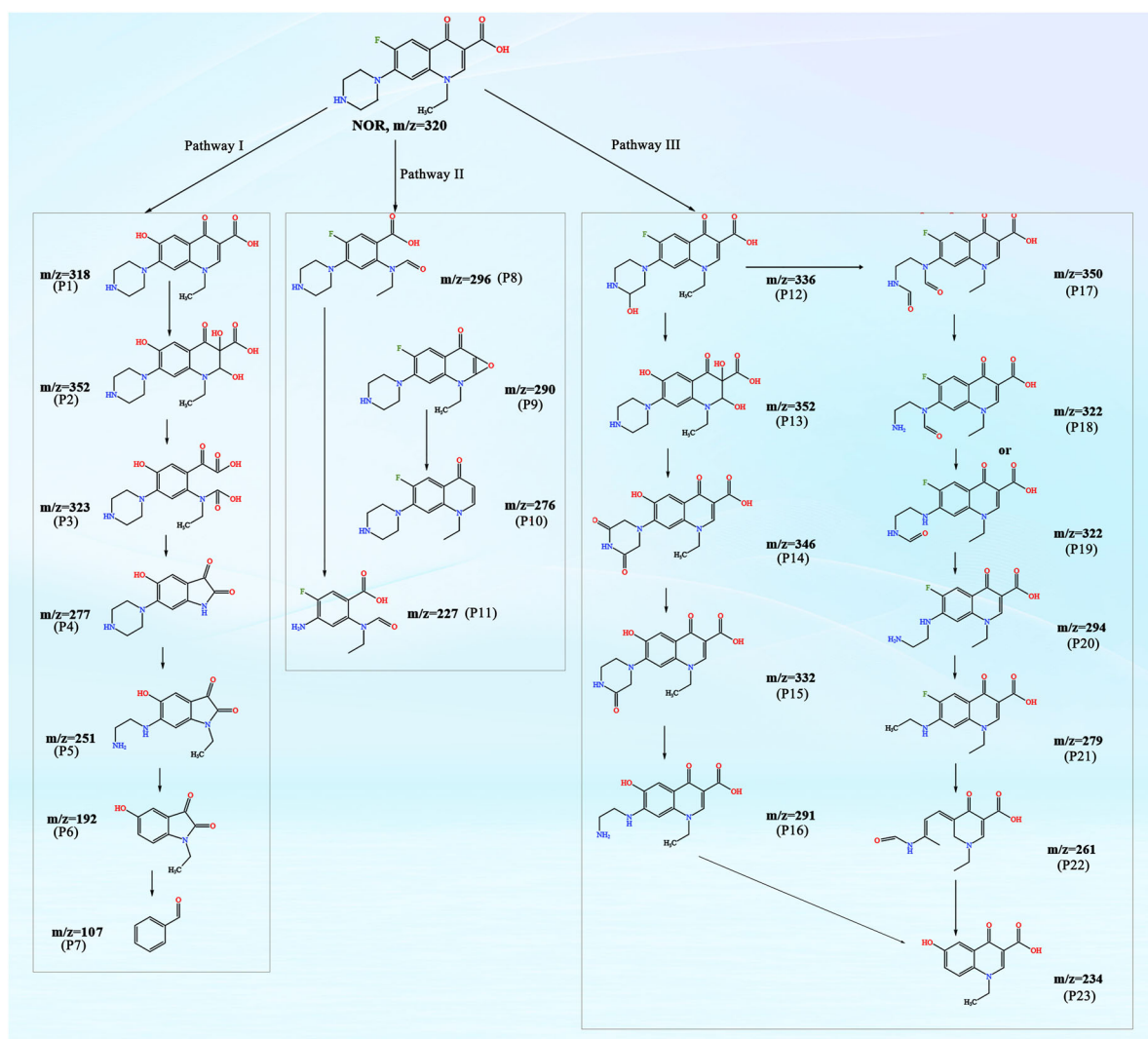


Fig. 14 | The possible photocatalytic degradation pathways of NOR by N,S-Ag<sub>3</sub>PO<sub>4</sub>@ACB.

affecting NOR degradation were analyzed. After five cycles, the degradation rate of N,S-Ag<sub>3</sub>PO<sub>4</sub>@ACB on NOR decreased by 10.08%; however, the structure did not change markedly. N,S-Ag<sub>3</sub>PO<sub>4</sub>@ACB effectively degraded NOR during wastewater treatment. The photocatalytic system was dominated by the oxidation of ·O<sub>2</sub><sup>-</sup>, H<sup>+</sup>, and ·OH with the Z-scheme photo-generated carrier transfer mode. Moreover, the activation of graphitic N and the lone electron pairs of N and S promoted rapid photogenerated charge transfer. The surface properties (EPRs and defects) of the ACB carrier promoted ROS generation, and the SPR effect of the Ag nanoparticles synergistically enhanced the photocatalytic activity of N,S-Ag<sub>3</sub>PO<sub>4</sub>@ACB. Furthermore, the degradation of NOR was recorded using 3D EEMs with three possible degradation pathways identified. The pathways were mainly associated with reactions such as replacement and elimination of F atoms, oxidative cleavage of the piperazine ring, decarboxylation and dealkylation, transformation of quinolone moieties, and ring opening. This study provides insights for the design of novel Ag-based composite photocatalysts with a Z-scheme and enriches the basic theory of the synergistic enhancement of photocatalytic mechanisms by N and S co-doping and biochar.

### Data availability

The data that support the findings of this study are available from the corresponding author upon reasonable request.

Received: 14 May 2024; Accepted: 11 September 2024;

Published online: 28 September 2024

### References

- Zainab, S. M., Junaid, M., Xu, N. & Malik, R. N. Antibiotics and antibiotic resistant genes (ARGs) in groundwater: a global review on dissemination, sources, interactions, environmental and human health risks. *Water Res.* **187**, 116455 (2020).
- Holmes, B., Brogden, R. & Richards, D. Norfloxacin: a review of its antibacterial activity, pharmacokinetic properties and therapeutic use. *Drugs* **30**, 482–513 (1985).
- Bhatt, S. & Chatterjee, S. Fluoroquinolone antibiotics: occurrence, mode of action, resistance, environmental detection, and remediation—A comprehensive review. *Environ. Pollut.* **315**, 120440 (2022).
- Shurbaji, S., Huong, P. T. & Altahtamouni, T. M. Review on the visible light photocatalysis for the decomposition of ciprofloxacin, norfloxacin, tetracyclines, and sulfonamides antibiotics in wastewater. *Catalysts* **11**, 437 (2021).
- Montañés, M. T. et al. Analysis of norfloxacin ecotoxicity and the relation with its degradation by means of electrochemical oxidation using different anodes. *Ecotoxicol. Environ. Saf.* **188**, 109923 (2020).
- Li, J. et al. Improving photocatalytic activity by construction of immobilized Z-scheme CdS/Au/TiO<sub>2</sub> nanobelt photocatalyst for eliminating norfloxacin from water. *J. Colloid Interface Sci.* **586**, 243–256 (2021).
- Wang, T. et al. Efficient visible-light photocatalysis of chloramphenicol using novel engineered biochar-based Ti-doped Bi<sub>2</sub>WO<sub>6</sub> composite: mechanisms, degradation pathways, and applications. *Sep. Purif. Technol.* **332**, 125780 (2024).
- Yi, Z. et al. An orthophosphate semiconductor with photooxidation properties under visible-light irradiation. *Nat. Mater.* **9**, 559–564 (2010).
- Wang, T. et al. Comparative study of enhanced adsorption-photodegradation activity using activated biochar composited with Ag<sub>3</sub>PO<sub>4</sub> or Ag<sub>6</sub>Si<sub>2</sub>O<sub>7</sub> in wastewater treatment and disinfection: effects and mechanisms. *Colloids Surf. A Physicochem. Eng. Asp.* **655**, 130235 (2022).
- Naciri, Y. et al. Photocatalytic oxidation of pollutants in gas-phase via Ag<sub>3</sub>PO<sub>4</sub>-based semiconductor photocatalysts: recent progress, new trends, and future perspectives. *Crit. Rev. Environ. Sci. Technol.* **52**, 2339–2382 (2022).
- Zhuang, H. et al. State-of-the-art progress in Ag<sub>3</sub>PO<sub>4</sub>-based photocatalysts: rational design, regulation and perspective. *Appl. Mater. Today* **31**, 101742 (2023).
- Amirulysyafiee, A., Khan, M. M. & Harunsani, M. H. Ag<sub>3</sub>PO<sub>4</sub> and Ag<sub>3</sub>PO<sub>4</sub>-based visible light active photocatalysts: Recent progress, synthesis, and photocatalytic applications. *Catal. Commun.* **172**, 106556 (2022).
- Wang, T. et al. Facile synthesis of activated biochar/BiVO<sub>4</sub> heterojunction photocatalyst to enhance visible light efficient degradation for dye and antibiotics: applications and mechanisms. *J. Mater. Res. Technol.* **19**, 5017–5036 (2022).
- Sharma, G. et al. Remediation of antibiotics using coordination polymers. *Coord. Chem. Rev.* **519**, 216120 (2024).
- Wei, X. et al. Porous biochar supported Ag<sub>3</sub>PO<sub>4</sub> photocatalyst for “two-in-one” synergistic adsorptive-photocatalytic removal of methylene blue under visible light irradiation. *J. Environ. Chem. Eng.* **9**, 106753 (2021).
- Bu, X. et al. Fabrication of novel Z-scheme LaCoO<sub>3</sub>/activated biochar/Ag<sub>3</sub>PO<sub>4</sub> heterojunctions for intensifying visible-light-catalytic degradation of bisphenol A. *Appl. Surf. Sci.* **588**, 152887 (2022).
- Ma, Y. et al. Fabrication of Ag<sub>3</sub>PO<sub>4</sub>/polyaniline-activated biochar photocatalyst for efficient triclosan degradation process and toxicity assessment. *Sci. Total Environ.* **821**, 153453 (2022).
- Talukdar, K. et al. Novel Z-scheme Ag<sub>3</sub>PO<sub>4</sub>/Fe<sub>3</sub>O<sub>4</sub>-activated biochar photocatalyst with enhanced visible-light catalytic performance toward degradation of bisphenol A. *J. Hazard. Mater.* **398**, 123025 (2020).
- Zhai, Y. et al. Novel biochar@CoFe<sub>2</sub>O<sub>4</sub>/Ag<sub>3</sub>PO<sub>4</sub> photocatalysts for highly efficient degradation of bisphenol a under visible-light irradiation. *J. Colloid Interface Sci.* **560**, 111–121 (2020).
- Qian, Y. et al. Integration of biochar into Ag<sub>3</sub>PO<sub>4</sub>/α-Fe<sub>2</sub>O<sub>3</sub> heterojunction for enhanced reactive oxygen species generation towards organic pollutants removal. *Environ. Pollut.* **303**, 119131 (2022).
- Li, X. et al. Application of silver phosphate-based photocatalysts: barriers and solutions. *Chem. Eng. J.* **366**, 339–357 (2019).
- Devi, L. G. & Kavitha, R. A review on non metal ion doped titania for the photocatalytic degradation of organic pollutants under UV/solar light: Role of photogenerated charge carrier dynamics in enhancing the activity. *Appl. Catal. B Environ.* **140**, 559–587 (2013).
- Wu, W. et al. Rational electron tuning of magnetic biochar via N, S co-doping for intense tetracycline degradation: Efficiency improvement and toxicity alleviation. *Chem. Eng. J.* **458**, 141470 (2023).
- Piątkowska, A., Janus, M., Szymański, K. & Mozia, S. C-, N- and S-doped TiO<sub>2</sub> photocatalysts: a review. *Catalysts* **11**, 144 (2021).
- Mao, W. et al. Facile assembled N, S-codoped corn straw biochar loaded Bi<sub>2</sub>WO<sub>6</sub> with the enhanced electron-rich feature for the efficient photocatalytic removal of ciprofloxacin and Cr (VI). *Chemosphere* **263**, 127988 (2021).
- Shabir, M. et al. Carbon nanotubes loaded N, S-codoped TiO<sub>2</sub>: Heterojunction assembly for enhanced integrated adsorptive-photocatalytic performance. *J. Ind. Eng. Chem.* **105**, 539–548 (2022).
- Anfar, Z. et al. New functionalization approach synthesis of Sulfur doped, Nitrogen doped and Co-doped porous carbon: superior metal-free Carbocatalyst for the catalytic oxidation of aqueous organics pollutants. *Chem. Eng. J.* **405**, 126660 (2021).
- Tian, J. et al. Anion-exchange synthesis of Ag<sub>2</sub>S/Ag<sub>3</sub>PO<sub>4</sub> core/shell composites with enhanced visible and NIR light photocatalytic performance and the photocatalytic mechanisms. *Appl. Catal. B Environ.* **209**, 566–578 (2017).
- Liang, C. et al. Boosting molecular oxygen activation ability in self-assembled plasmonic p-n semiconductor photocatalytic heterojunction of WO<sub>3</sub>/Ag@Ag<sub>2</sub>O. *Chem. Eng. J.* **372**, 12–25 (2019).
- Liu, Y. et al. Fabrication, application, and mechanism of metal and heteroatom co-doped biochar composites (MHBCs) for the removal

- of contaminants in water: a review. *J. Hazard. Mater.* **431**, 128584 (2022).
31. Alshamsi, H. A., Beshkar, F., Amiri, O. & Salavati-Niasari, M. Porous hollow Ag/Ag<sub>2</sub>S/Ag<sub>3</sub>PO<sub>4</sub> nanocomposites as highly efficient heterojunction photocatalysts for the removal of antibiotics under simulated sunlight irradiation. *Chemosphere* **274**, 129765 (2021).
  32. Cai, T. et al. A promising inorganic-organic Z-scheme photocatalyst Ag<sub>3</sub>PO<sub>4</sub>/PDI supermolecule with enhanced photoactivity and photostability for environmental remediation. *Appl. Catal. B Environ.* **263**, 118327 (2020).
  33. Shi, E. et al. Ag<sub>2</sub>S-doped core-shell nanostructures of Fe<sub>3</sub>O<sub>4</sub>@Ag<sub>3</sub>PO<sub>4</sub> ultrathin film: major role of hole in rapid degradation of pollutants under visible light irradiation. *Chem. Eng. J.* **366**, 123–132 (2019).
  34. Gao, Q., Xu, J., Wang, Z. & Zhu, Y. Enhanced visible photocatalytic oxidation activity of perylene diimide/g-C<sub>3</sub>N<sub>4</sub> n-n heterojunction via  $\pi$ - $\pi$  interaction and interfacial charge separation. *Appl. Catal. B Environ.* **271**, 118933 (2020).
  35. Yuan, J., Wen, Y., Dionysiou, D. D., Sharma, V. K. & Ma, X. Biochar as a novel carbon-negative electron source and mediator: electron exchange capacity (EEC) and environmentally persistent free radicals (EPFRs): a review. *Chem. Eng. J.* **429**, 132313 (2022).
  36. Ma, P. et al. Assembly of Ag<sub>3</sub>PO<sub>4</sub> nanoparticles on two-dimensional Ag<sub>2</sub>S sheets as visible-light-driven photocatalysts. *Phys. Chem. Chem. Phys.* **18**, 3638–3643 (2016).
  37. Martin, D. J. et al. Efficient visible driven photocatalyst, silver phosphate: performance, understanding and perspective. *Chem. Soc. Rev.* **44**, 7808–7828 (2015).
  38. Dong, Y., Su, Y., Hu, Y., Li, H. & Xie, W. Ag<sub>2</sub>S-CdS p-n nanojunction-enhanced photocatalytic oxidation of alcohols to aldehydes. *Small* **16**, 2001529 (2020).
  39. Meng, S., Zhang, J., Chen, S., Zhang, S. & Huang, W. Perspective on construction of heterojunction photocatalysts and the complete utilization of photogenerated charge carriers. *Appl. Surf. Sci.* **476**, 982–992 (2019).
  40. Chen, M. & Chu, W. Photocatalytic degradation and decomposition mechanism of fluoroquinolones norfloxacin over bismuth tungstate: experiment and mathematic model. *Appl. Catal. B Environ.* **168**, 175–182 (2015).
  41. Shah, N. S. et al. Solar light driven degradation of norfloxacin using as-synthesized Bi<sup>3+</sup> and Fe<sup>2+</sup> co-doped ZnO with the addition of HSO<sub>5</sub><sup>-</sup>: Toxicities and degradation pathways investigation. *Chem. Eng. J.* **351**, 841–855 (2018).
  42. Ding, D. et al. Mechanism insight of degradation of norfloxacin by magnetite nanoparticles activated persulfate: identification of radicals and degradation pathway. *Chem. Eng. J.* **308**, 330–339 (2017).

## Acknowledgements

This research was funded by the following grants, including the Key Research and Development Program of Shaanxi Province (No. 2023-LL-QY-42, 2024NC-ZDCYL-02-05), the Xi'an University of Architecture and

Technology Research Initiation Grant Program (No. 1960323102), the Xi'an University of Architecture and Technology Special Program for Cultivation of Frontier Interdisciplinary Fields (No. X20230079), and the Open Fund for the Key Laboratory of Soil and Plant Nutrition of Ningxia (No. ZHS202401). The authors also thank Shiyanjia Lab ([www.shiyanjia.com](http://www.shiyanjia.com)) for the support of the specific surface area tests.

## Author contributions

All authors contributed to this study. Tongtong Wang: Methodology, Software, Conceptualization, Data curation, Visualization, Formal analysis, Funding acquisition, Project administration, and Writing-original draft. Amit Kumar and Gaurav Sharma: Writing-review & editing. Sen Wang and Junchao Jia: Validation and Investigation. Jiyong Zheng: Resources, Writing-review & editing. Hui Shi: Resources, Supervision, Funding acquisition, and Writing-review & editing.

## Competing interests

The authors declare no competing interests.

## Additional information

**Supplementary information** The online version contains supplementary material available at <https://doi.org/10.1038/s41545-024-00393-8>.

**Correspondence** and requests for materials should be addressed to Tongtong Wang or Hui Shi.

**Reprints and permissions information** is available at <http://www.nature.com/reprints>

**Publisher's note** Springer Nature remains neutral with regard to jurisdictional claims in published maps and institutional affiliations.

**Open Access** This article is licensed under a Creative Commons Attribution-NonCommercial-NoDerivatives 4.0 International License, which permits any non-commercial use, sharing, distribution and reproduction in any medium or format, as long as you give appropriate credit to the original author(s) and the source, provide a link to the Creative Commons licence, and indicate if you modified the licensed material. You do not have permission under this licence to share adapted material derived from this article or parts of it. The images or other third party material in this article are included in the article's Creative Commons licence, unless indicated otherwise in a credit line to the material. If material is not included in the article's Creative Commons licence and your intended use is not permitted by statutory regulation or exceeds the permitted use, you will need to obtain permission directly from the copyright holder. To view a copy of this licence, visit <http://creativecommons.org/licenses/by-nc-nd/4.0/>.

© The Author(s) 2024